Thesis for The Degree of Licentiate of Engineering

Modelling and optimization of runaway electrons in tokamaks

Ida Ekmark

Department of Physics
Chalmers University of Technology
Gothenburg, Sweden, 2025

Modelling and optimization of runaway electrons in tokamaks

Ida Ekmark

Plasma Theory research group
Division of Subatomic, High Energy and Plasma Physics
Department of Physics
Chalmers University of Technology
SE-412 96 Göteborg
Sweden
Phone: +46(0)31 772 1000

Cover:
An illustration of the increasing runaway current density in a tokamak plasma. The sequential poloidal slices of the plasma torus illustrate the runaway current density as it increases with time during a disruption in SPARC. The runaway current density data used comes from a disruption simulation in paper D.

Printed by Chalmers Digitaltryck,
Gothenburg, Sweden 2025.

Modelling and optimization of runaway electrons in tokamaks

Ida Ekmark

Department of Physics
Chalmers University of Technology

Abstract

During tokamak start-up and disruptions, strong electric fields can arise which are sufficient to cause electron runaway, whereby electrons are accelerated continuously. In future large-current tokamaks, such as ITER and SPARC, significant runaway electron generation is expected. Should the runaway electron beam come in contact with the tokamak wall, its energy can be almost instantly deposited into the wall. After a disruption, a considerable fraction of the plasma current could be carried by relativistic electrons, which could seriously damage the device. Start-up runaway electrons also risk causing damage to the tokamak, but can also impede the plasma initiation. Electron runaway is one of the major unsolved challenges in the development of fusion as a viable source of energy. This thesis focuses on accurate modelling of tokamak start-up and disruptions as well as the optimization of disruption mitigation, centering especially around runaway electrons.

The simulation tool Stream has been developed for studying runaway electrons during the burn-through and ramp-up phases of tokamak start-up. Stream uses a 0D plasma model, where the densities, currents, temperatures and electric field are evolved self-consistently. The runaway electron evolution is governed by Dreicer and avalanche generation, as well as particle transport. Using Stream, it was found that Dreicer generation plays a crucial role for start-up runaway dynamics, and can even dominate the runaway generation.

Fluid and kinetic modelling of the runaway seed generation during tokamak disruptions have been compared. It was found that the two models can give significantly different predictions of the runaway evolution. The largest difference found concerned the hot-tail generation, as the neglect of radial transport in the fluid model caused a significant overestimation of the runaway generation rate. Kinetic modelling of the seed generation was thus found to be preferable, despite the increased computational cost.

Disruption optimizations for both ITER and SPARC were performed, focused on minimizing heat loads, electromechanical forces and the runaway current. More specifically, the injected densities of deuterium and noble gases during massive material injection were optimized. For ITER, simultaneous minimization of all three objectives was found to be possible only in pure deuterium plasmas. During activated operation, low runaway currents always correlated with large transported heat losses. For SPARC, successful mitigation was found to be feasible in deuterium-tritium plasmas as well.

Keywords: Plasma physics, fusion, tokamak, runaway electrons, start-up, disruption mitigation

List of Publications

Appended publications

A M. Hoppe, I. Ekmark, E. Berger and T. Fülöp,
Runaway electron generation during tokamak start-up
Journal of Plasma Physics **88** 905880317 (2022).
https://doi.org/10.1017/S002237782200054X

B I. Pusztai, I. Ekmark, H. Bergström, P. Halldestam, P. Jansson, M. Hoppe, O. Vallhagen and T. Fülöp,
Bayesian optimization of massive material injection for disruption mitigation in tokamaks
Journal of Plasma Physics **89** 905890204 (2023).
https://doi.org/10.1017/S0022377823000193

C I. Ekmark, M. Hoppe, T. Fülöp, P. Jansson, L. Antonsson, O. Vallhagen and I. Pusztai,
Fluid and kinetic studies of tokamak disruptions using Bayesian optimization
Journal of Plasma Physics **90** 905900306 (2024).
https://doi.org/10.1017/s0022377824000606

D I. Ekmark, M. Hoppe, R. A. Tinguely, R. Sweeney, T. Fülöp and I. Pusztai,
Runaway electron generation in disruptions mitigated by deuterium and noble gas injection in SPARC
Accepted for publication in Journal of Plasma Physics.
https://arxiv.org/abs/2502.19891

Related publications, not included in the thesis

E I. Ekmark, I. Pusztai, M. Hoppe, P. Jansson and T. Fülöp,
Bayesian optimization of disruption scenarios with fluid-kinetic models
Proceedings of the 49th EPS Conference on Plasma Physics, Bordeaux, P5-008 (2023).
https://lac913.epfl.ch/epsppd3/2023/html/Fr/Fr_MCF08_Ekmark.pdf

F J. Walkowiak, M. Hoppe, I. Ekmark, A. Jardin, J. Bielecki, K. Król, Y. Savoye-Peysson, D. Mazon, D. Dworak and M. Scholz,
First numerical analysis of runaway electron generation in tungsten-rich plasmas towards ITER
Nuclear Fusion **64** 036024 (2024).
https://doi.org/10.1088/1741-4326/ad24a0

G I. Ekmark, M. Hoppe, T. Fülöp, R.A. Tinguely, R. Sweeney, P. Jansson, L. Antonsson, O. Vallhagen and I. Pusztai,
Fluid and kinetic modeling of runaway electron generation from tritium beta decay and Compton scattering
Proceedings of the 50th EPS Conference on Plasma Physics, Salamanca, P4-109 (2024).
https://lac913.epfl.ch/epsppd3/2024/html/PDF/P4-109.pdf

Statement of contribution

Paper A I implemented the STREAM code together with M. Hoppe and E. Berger. I benchmarked the code in close collaboration with M. Hoppe. Furthermore, I performed the simulations and created all the figures of sections 3 and 4, and contributed to the analysis of the simulations.

Paper B After initial optimization algorithm implementation by H. Bergström and P. Halldestam, I reproduced and refined their code and results. The code developed by me was used to produce the optimization data set of the paper. I also created figure 1 of the paper.

Paper C I implemented the optimization algorithms used and performed the optimizations, as well as the additional simulations. I created all the figures, and analyzed and discussed the results in close collaboration with the co-authors. Furthermore, I derived the kinetic sources used for the reduced kinetic simulations, with assistance from M. Hoppe. The majority of the manuscript was written by me, with support from the co-authors.

Paper D Using the optimization algorithm I developed for paper C, I performed all the optimizations and simulations, based on machine parameters, initial profiles and data for the photon flux spectra of SPARC obtained from A. Tinguely and R. Sweeney. The results were analyzed and discussed in close collaboration with the co-authors. I created all the figures and wrote the manuscript.

Acknowledgements

I feel incredibly grateful and fortunate for being a part of the Plasma Theory research group, and getting to know and work with the extraordinary members of the runaway electron and plasma physics communities.

First of all, I would like to express my deepest gratitude to my main supervisor, Tünde Fülöp, for bringing me into this community and guiding me on my academic journey. I am repeatedly amazed at the support she provides and the effort she invests in making sure I reach my highest potential, as well as all the opportunities I am presented with, thanks to her dedication. Never could I have hoped for a better supervisor and role model.

I would also like to show appreciation to my supervisor István Pusztai, for answering my questions, without exception, regardless of if they are related to physics, writing or academia in general. Furthermore, I feel very fortunate for his commitment to my academic success and development.

Likewise, I would like to thank my supervisor Mathias Hoppe, for always taking the time to discuss my problems, as well as ideas and future projects. I am very grateful to have a mentor like him, who challenges and inspires me to become a better physicist and researcher.

For elevating my every day working experience, I would like to thank my fellow group members, both past and present, among them: Andréas, Björn, Dominika, Emil, Konrad, Mufei and Oskar. The daily interactions, companionship and support you provide makes every day an enjoyable experience and something to look forward to.

Through this journey, I have had the opportunity to work with a number of excellent and inspiring people, and I am grateful for their support and collaboration: Alex Tinguely, Esmée Berger, Hannes Bergström, Patrik Jansson, Peter Halldestam and Ryan Sweeney. Additionally, I would like to extend my warm gratitude to Sarah Newton, for selflessly taking the time to thoroughly read and comment on my academic texts.

Finally, I would like to thank my family and friends, for their constant support and encouragement, as well as giving purpose and joy outside of the bubble that is academia.

Ida Ekmark, Göteborg, April 2025

Contents

Part I

Introduction

Chapter 1

Introduction

As our society progresses and we raise the standard of living around the world, our energy consumption will also increase [1]. In order to maintain this positive progression, our energy production needs to be sustainable to use long term. Today, our main forms of energy production generate unacceptable levels of green house gas emissions or long-lived nuclear waste. One of the greatest challenges of the 21st century is to develop reliable sources of energy which can cover our increasing energy needs without burdening the environment. A potential candidate for such an energy source is nuclear fusion, namely utilizing the release of energy from two lighter nuclei fusing into one.

Nuclear fusion power plants would use the heavy hydrogen isotopes deuterium and tritium as fuel. Deuterium can be found in water and is abundant in our oceans, while tritium can be produced from lithium, which can be sourced from both land-based reserves and the ocean. This, combined with the high energy to fuel mass ratio, means that nuclear fusion can theoretically provide us with sustainable energy for thousands to millions of years [2].

The main by-product of the fusion reaction is the stable isotope helium-4, meaning there would be no significant green house gas emissions [2]. In terms of harmful by-products, the walls will be activated by the neutron emitted during the fusion reaction, but the radioactive material would be short-lived. For fusion reactors, the storage requirements would thus be more relaxed compared to those for the nuclear waste of fission reactors. Furthermore, it would be a non-intermittent energy source since it is not dependent on any fluctuating and unpredictable factor such as the weather [3]. Consequently, fusion would be an ideal source of energy if its development succeeds.

Although nuclear fusion is a prevalent phenomenon in our universe, as it is the energy source that powers the sun and the stars, creating the conditions necessary to produce significant levels of fusion energy in an artificial environment is complicated. Notably, the fuel has to be heated to more than hundreds of million degrees in order for the fusion reaction to occur with high enough frequency [2], and at such temperatures the atoms of the fuel separates into ions and free electrons – the fuel is in the plasma phase. This introduces the

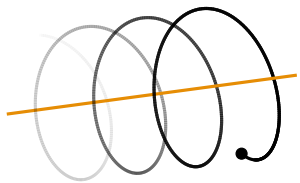

Figure 1.1: In the presence of a homogeneous and static magnetic field, a charged particle (black) gyrates around a magnetic field line (orange).

first problem of achieving fusion – confining the fuel for long enough periods of time to produce significant levels of energy.

One of the most widely researched solutions for this is the tokamak, which is a machine that uses magnetic fields to confine the heated fuel in the shape of a torus. The characteristic feature of the tokamak is that it produces the necessary magnetic field by combining magnetic field coils with a large current driven through the plasma [4]. The plasma current is crucial for the confinement of the fuel in a tokamak, but it does not come without complications – one of them is the risk of producing relativistic electrons, so called runaway electrons, capable of damaging the machine itself [5]. Significant generation of runaway electrons can occur either during the plasma current ramp-up (start-up of the tokamak) or during sudden plasma terminating events (disruption). How to mitigate or avoid the generation of runaway electrons in tokamaks is considered one of the most critical, unresolved problems of the tokamak concept.

1.1 Basic plasma physics

A plasma is defined as a macroscopically neutral gas consisting of charged particles, where the particle dynamics are governed by both short- and long-range particle interactions [6]. Locally, the particle dynamics are affected by collisions with other particles, but long-range forces arise from the electromagnetic fields of the charged particles, and the dynamics is also heavily influenced by externally applied fields. In the presence of an electric field $\boldsymbol{E}$ and a magnetic field $\boldsymbol{B}$, a particle of charge q and velocity $\boldsymbol{v}$ experiences the Lorentz force

$$\boldsymbol{F} = q\left(\boldsymbol{E} + \boldsymbol{v} \times \boldsymbol{B}\right). \tag{1.1}$$

If there is only an electric field present, the charged particle is accelerated parallel to the electric field. On the other hand, if the charged particle is only in the presence of a homogeneous and static magnetic field, it gyrates around the magnetic field line with constant speed, according to the second term in (1.1). More specifically, the charged particle follows a helical orbit with the guiding centre, namely the line traced out by the centre of the circular motion, aligned with the magnetic field line, see figure 1.1. The radius of this circular motion is called the Larmor radius, given by

$$r_{\mathrm{L}} = \frac{m v_{\perp}}{|q| B}, \tag{1.2}$$

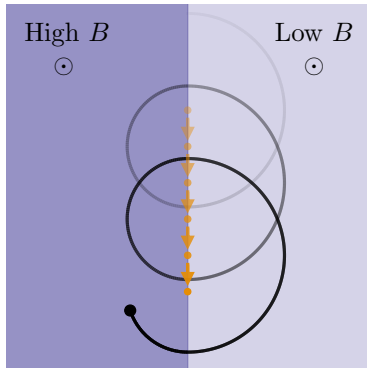

Figure 1.2: As a charged particle travels through a region of higher and of lower magnetic field strength, it drifts due to the difference in Larmor radius of its circular orbit in the two different regions – note the vertical displacement of the guiding centre (orange dot). The direction of the magnetic field is orthogonal to the plotted plane.

with m and $v_\perp$ being the mass and perpendicular speed of the particle, and B being the strength of the magnetic field.

However, if the charged particle is affected both by a magnetic field and some other force, e.g. an electric field, and if the two are not parallel, the guiding centre drifts orthogonally to both the magnetic field and the force. Magnetic field inhomogeneities or time-varying fields also cause the guiding centre to drift. As a simplified illustration, if the guiding centre of a charged particle would be located at the boundary between two regions of different magnetic field strength, the Larmor radius would be smaller in the region of higher magnetic field strength, which would cause the particle to drift in accordance with figure 1.2.

The most accurate approach of modelling a plasma would be to consider the dynamics of each particle in the plasma, accounting for all of the electromagnetic forces acting on each particle at any given time, including the forces from the electric fields of all other charged particles [6]. However, these single-particle models are computationally intractable, since the numerical complexity of modelling interactions of all particle pairs is proportional to (at least) N^2, where N is the number of particles, and for a typical fusion plasma $N > 10^{20}$.

To make the problem tractable, one can model the plasma based on the collective behaviour of the charged particles as a group, and the most fundamental such model is the kinetic plasma model. In the kinetic model, the plasma is described statistically by a distribution function $f(\boldsymbol{r}, \boldsymbol{v}, t)$. It is defined such that $f(\boldsymbol{r}, \boldsymbol{v}, t)\mathrm{d}\boldsymbol{r}\mathrm{d}\boldsymbol{v}$ represents the number of particles within the six-dimensional volume-element $\mathrm{d}\boldsymbol{r}\mathrm{d}\boldsymbol{v}$ in position and velocity space (or, equivalently, momentum space). The evolution of the distribution function is governed by the Boltzmann equation [6]

$$\frac{\partial f}{\partial t} + \boldsymbol{v} \cdot \boldsymbol{\nabla} f + \frac{\boldsymbol{F}}{m} \cdot \boldsymbol{\nabla}_{\boldsymbol{v}} f = \left(\frac{\partial f}{\partial t} \right)_{\mathrm{c}}, \tag{1.3}$$

where $(\partial f/\partial t)_\mathrm{c}$ is a collision operator and the force $\boldsymbol{F}$ can be replaced by the Lorentz force in equation (1.1) if it is purely electromagnetic. The distribution function gives a dense description the plasma, but more easily-interpretable quantities can be obtained from the velocity moments of the distribution function, such as [7]

$$\text{Density: } n(\boldsymbol{r},t) = \int f(\boldsymbol{r},\boldsymbol{v},t)\mathrm{d}\boldsymbol{v}, \tag{1.4a}$$

$$\text{Mean velocity: } \boldsymbol{u}(\boldsymbol{r},t) = \frac{1}{n}\int \boldsymbol{v} f(\boldsymbol{r},\boldsymbol{v},t)\mathrm{d}\boldsymbol{v}, \tag{1.4b}$$

$$\text{Temperature: } T(\boldsymbol{r},t) = \frac{2}{3n}\int \frac{m}{2}|\boldsymbol{v}-\boldsymbol{u}|^2 f(\boldsymbol{r},\boldsymbol{v},t)\mathrm{d}\boldsymbol{v}. \tag{1.4c}$$

The distribution function describing a non-relativistic plasma in local thermodynamic equilibrium is the Maxwell-Boltzmann distribution [6]

$$f_\mathrm{M} \propto \left(\frac{1}{\sqrt{\pi}v_\mathrm{th}}\right)^3 \exp\left(-\frac{v^2}{v_\mathrm{th}^2}\right). \tag{1.5}$$

Here, the so called thermal speed $v_\mathrm{th} = (2T/m)^{1/2}$ determines the width of the distribution, where T (measured in units of energy, typically eV) is the temperature of the particle species and m the particle mass.

The effect of collisions on the distribution function evolution is accounted for using the collision operator, but a complete description encompassing all forms of Coulomb interactions in a plasma is generally intractable. A commonly used collision operator in fusion plasmas is the Fokker-Planck operator, which assumes that the plasma dynamics are dominated by long-range Coulomb collisions, which only cause small relative changes of the respective velocities. The resulting equation is known as the Fokker-Planck equation, and it describes the effect of collisions on particle species i with [7, 8]

$$\left(\frac{\partial f}{\partial t}\right)_\mathrm{c}^i = \sum_j \frac{\partial}{\partial \boldsymbol{v}} \cdot \left[-\boldsymbol{A}^{ij} f + \mathbb{D}^{ij} \cdot \frac{\partial f}{\partial \boldsymbol{v}}\right], \tag{1.6}$$

where the sum runs over all particle species j. Here $\boldsymbol{A}^{ij}$ represents the average force felt by a particle of species i due to collisions with particles of species j, and $\mathbb{D}^{ij}$ is a diffusion tensor [7].

A less accurate but computationally much more efficient approach is to integrate over the details of the phase space dynamics and treat them as fluids. The fluid model simplifies the kinetic theory, using velocity moments, to describe the plasma constituents by fluid quantities (see (1.4)) and govern the evolution by a set of so called fluid equations [6]. Using a fluid model greatly reduces the complexity found in the kinetic model – the kinetic model describes up to six dimensions while the fluid model considers at most three – but the detailed description of processes in the velocity space is lost.

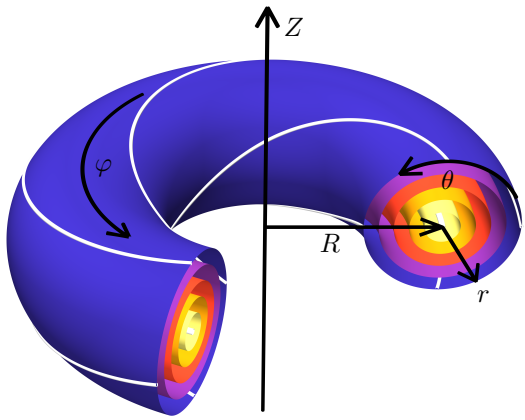

Figure 1.3: Illustration of the tokamak geometry. Commonly, a toroidal coordinate system is used for tokamaks, with the minor radius r, and the poloidal and toroidal angle coordinates θ and φ. Additionally, the toroidal coordinate forms a cylindrical coordinate system together with the major radial coordinate R and vertical coordinate Z. The coloured torus surfaces represent nested flux surfaces. The twist of the magnetic field lines is illustrated by the white curves on the outermost flux surface.

1.2 Tokamak concept

One of the most promising fusion reactor concepts is the tokamak, which uses magnetic fields to confine the fusion plasma. External magnetic field coils create a toroidal magnetic field with the purpose of guiding the charged particles around the tokamak in confined loops. The plasma is thus in the shape of a torus, as illustrated in figure 1.3. However, such a magnetic field exhibits spatial inhomogeneities, and the strength of this field approximately varies as $1/R$ [4], causing vertical drifts of the particles and, without any additional measures taken, intolerable particle losses. The direction of the drift due to the spatial gradients in a tokamak only depends on the charge of the particle, and since the charge of the particle does not change, neither does the direction of the drift [4]. Consequently, the direction of this vertical drift is the same on both the upper and lower halves of the plasma torus.

One simple solution to this problem of particle losses caused by the spatial magnetic field gradients is to introduce a poloidal magnetic field, which allows the magnetic field lines to be twisted around the torus, as illustrated by the white lines on the outer (blue) surface of figure 1.3. Notably, in a tokamak, the poloidal field is weaker than the toroidal field. If the particle drifts away from the plasma column in the upper half of the plasma torus, it drifts towards the plasma column on the lower half and these drifts cancel out as the particle moves along the twisted magnetic field. In a tokamak the poloidal magnetic field is produced by driving a toroidal plasma current of several mega-amperes through the plasma.

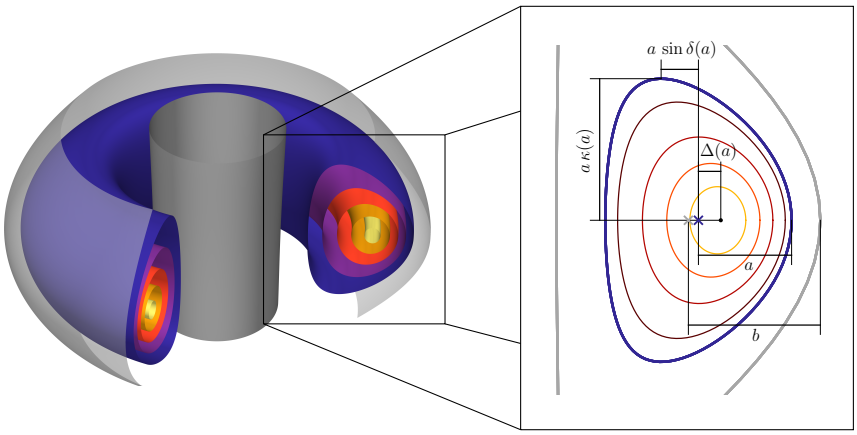

Figure 1.4: Shaping parameters for a tokamak; elongation $\kappa(r)$, triangularity $\delta(r)$ and Shafranov shift $\Delta(r)$ evaluated at the flux surface at $r = a$. The increasingly elongated and triangular oval shapes are nested flux surfaces, and the degenerate flux surface at $r = 0$ is marked with a black dot. The blue cross marks the centre of the outermost (blue) flux surface, with radius a (plasma minor radius). The gray cross marks the centre of the tokamak wall (gray), with wall radius b.

The twisted magnetic field lines trace out closed toroidal surfaces, so called flux surfaces [4]. In figure 1.3, nested flux surfaces are illustrated as the nested, coloured toroidal surfaces. The degenerate flux surface, located at $r = 0$, is called the magnetic axis. From the flux surfaces and magnetic axis we can define two characteristic geometric parameters for a tokamak – the major radius R_0 which is the distance between the vertical symmetry axis and the magnetic axis, as well as the minor radius a which is the radius of the outermost (closed) flux surface.

In practice, most tokamak plasmas do not have a circular cross section. Typically, the cross section shape of the flux surfaces is more triangular and vertically elongated compared to a circle. The actual flux surface geometry may be parametrized by the so called shaping parameters, which are illustrated in figure 1.4 together with the plasma minor radius a and wall radius b. Elongation is described by $\kappa(r)$ and triangularity by $\delta(r)$ – both of these are dimensionless quantities [9]. In this thesis, the Shafranov shift $\Delta(r)$ describes the horizontal displacement of the centre of a flux surface from the magnetic axis [4].

Tokamak start-up

The start-up of a tokamak can be divided into three phases – breakdown, burn-through and current ramp-up. Before initializing the breakdown phase, the vacuum chamber is filled with the plasma fuel at a predetermined density – the prefill density – or equivalently, at a predetermined pressure – prefill

pressure. A strong electric field is applied in the tokamak chamber, causing free electrons in the chamber to be accelerated. When the electrons have obtained enough energy (namely $> 13.6\,\text{eV}$), they can ionize atoms through collisions. The breakdown phase depends on there being an exponential increase in the number of free electrons produced by free electrons colliding with atoms – this process is called the Townsend avalanche [10]. In order for the breakdown to be successful, the prefill density must be high enough so that there are enough target atoms for the electrons to collide with, to cause this exponentially increasing free electron density. However, if the prefill density is too high, or the electric field is insufficient, the free electrons will not gain enough energy before the collision to ionize the atom, meaning that the breakdown fails.

The ionization process is continued during the burn-through phase. At this point it is important for the heating of the plasma to be greater than the heat losses due to the ionization work and the collisional radiation [11]. Supplementary heating can then be used to ensure continued ionization. As the temperature in the plasma increases, the plasma resistivity decreases, leading to the plasma current being ramped up.

Disruptions in tokamaks

During tokamak operation, there can be unwanted *disruptions*. These events arise from instabilities in the plasma that cause a rapid loss of the plasma thermal energy. More specifically, such events are caused by instabilities that can be described by magnetohydrodynamics (MHD) [12]. MHD instabilities can be triggered, for example, by high currents, densities or pressures in the plasma, or by external causes associated with the tokamak hardware or operation [12].

Although disruptions can have a variety of causes, the macroscopic disruption evolution is qualitatively similar for most disruptions [4]. The typical chain of events is illustrated in figure 1.5. Initially, the temperature of the plasma decays rapidly, during what is called the *thermal quench* (TQ). For instance, the MHD instability causes the tokamak magnetic field lines to become stochastic (i.e. randomly wandering radially, instead of tracing out closed magnetic surfaces), causing heat to be transported to the inner tokamak wall [13]. Furthermore, the presence of impurities in the plasma can cause significant radiative heat losses, which also contributes to the temperature decay. The duration of the TQ is estimated to be $\sim 0.1\,\text{ms}$ for SPARC [14] and $\sim 1\,\text{ms}$ for ITER [15].

Since the resistivity of the plasma $\propto T^{-3/2}$, the plasma current starts to decay as a result of the thermal quench – this is the second phase of the disruption, known as the *current quench* (CQ). The decay of the current is a slower process than the temperature decay, for SPARC it is estimated to be $\sim 10\,\text{ms}$ and for ITER $\sim 100\,\text{ms}$. An electric field is induced by the decaying current, which can enable the generation of a significant current of relativistic electrons, also called runaway electrons. If a significant runaway current is generated and maintained, there is an additional phase of the disruption called the runaway plateau.

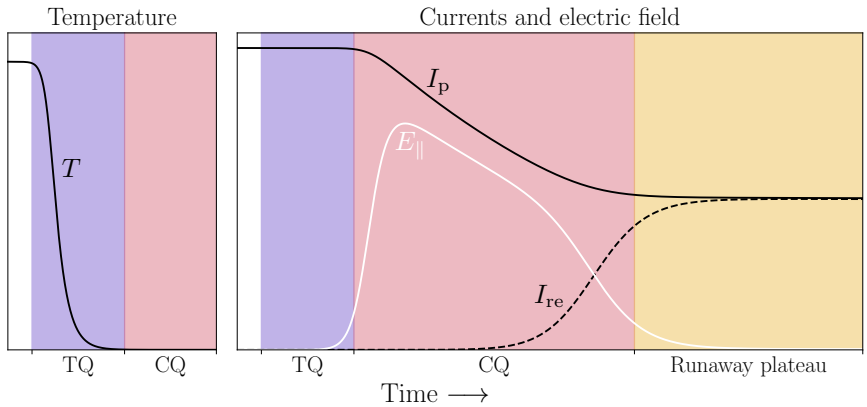

Figure 1.5: Illustration of the three important stages during a disruption. Firstly, the temperature decays during the thermal quench (TQ). Subsequently, and the plasma current decays during the current quench (CQ), which induces an electric field enabling a significant runaway current to be generated. If a significant runaway current is generated, it might reach a stable level during the stage known as the runaway plateau.

1.3 Runaway electrons

In a tokamak, electrons are accelerated by electric fields and are slowed down due to friction caused by collisions with other charged particles, i.e. Coulomb collisions. The equation of motion of a non-relativistic electron parallel to the magnetic field can be approximately written as

$$\frac{\mathrm{d}v_\parallel}{\mathrm{d}t} = -\frac{e}{m_\mathrm{e}} E_\parallel - \nu_\mathrm{c} v_\parallel, \tag{1.7}$$

where $E_\parallel < 0$ is the electric field component parallel to the magnetic field and ν_c is the collision frequency. Notably, the collision frequency ν_c depends non-monotonically on the velocity of the electron. As illustrated in figure 1.6, the friction force increases with speeds below the electron thermal speed ($v_\mathrm{th} = \sqrt{2T_\mathrm{e}/m_\mathrm{e}}$). However, for speeds above v_th, the friction starts to decrease with speed according to $\nu_\mathrm{c} \propto 1/v^3$. For a given electric field $E_\parallel$, there is a critical velocity v_c such that

$$-\frac{e}{m_\mathrm{e}} E_\parallel = \nu_\mathrm{c} v_\mathrm{c} \implies \frac{\mathrm{d}v_\parallel}{\mathrm{d}t} = 0. \tag{1.8}$$

Notably, for velocities above the critical velocity, the electric force becomes larger than the collisional friction forces, resulting in continuous acceleration. Electrons experiencing this kind of "unhindered"[1] acceleration due to the electric field are called runaway electrons and they are accelerated to relativistic speeds.

[1] It is worth noting, however, that this continuous acceleration is not completely unhindered – for very high velocities, it is limited by radiation effects (synchrotron and bremsstrahlung), which need to be accounted for by extending (1.7).

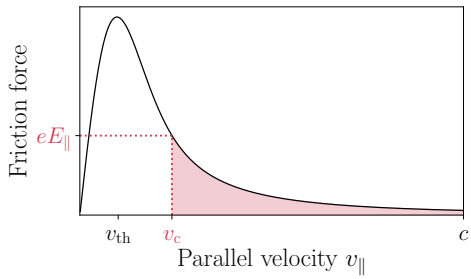

Figure 1.6: Illustration of the friction force due to Coulomb collisions on electrons in a fusion plasma, as a function of velocity. Electrons with velocities $v > v_{\mathrm{c}}$ run away.

For a tokamak discharge, sufficiently strong electric fields are present especially during the tokamak start-up or during disruptions. During tokamak start-up, a high electric field is applied to the initially neutral fuel gas in order to initiate the plasma [16]. Notably, for successful plasma initiation, the initial gas density needs to be relatively low, which correlates to low collisionality for the electrons in the plasma, which in turn reduces the electric field strengths needed for significant levels of runaway generation. On the other hand, during plasma disruptions, an electric field is induced as the plasma current starts to decay due to increased resistivity in the plasma. This induced electric field can be large enough such that a current of runaway electrons of similar order of magnitude as the original plasma current is generated, and survives even after the rest of the plasma current has decayed [5].

The issue with runaway electrons in tokamaks is that they can cause serious damage to the device [17]. A beam of runaway electrons can carry a large fraction of the stored magnetic energy, and if this beam would collide with the tokamak inner wall, it would deposit this energy in a localized area, which could cause major damage both to the plasma facing components as well as to structures behind the first wall tiles [17, 18].

In current tokamak experiments, runaway electrons are not considered a major problem [5], but this is not true for future devices. Runaway electrons are expected to pose a larger problem for future tokamaks because the avalanche gain is exponentially sensitive to the size of the plasma current during the discharge [19]. For reactor-scale tokamaks, the device size, and consequently the plasma current necessary, need to be significantly larger than the experimental devices that have been developed so far.

1.4 Thesis outline

In this thesis, we address the modelling and optimization of tokamak start-up and disruptions, with particular consideration of runaway electrons. We cover the different mechanisms of runaway generation in tokamaks in chapter 2 by

describing the underlying physics and presenting analytical formulas for the corresponding runaway generation rates. In chapter 3, we consider the context of runaway electrons in fusion plasmas, and present the plasma models used for studying runaway electrons during tokamak start-up and disruptions in this work. Aside from describing how runaway electrons fit in to the broader picture when modelling tokamak plasmas, we also present how the plasma evolution is self-consistently determined. Special focus is given to the key differences in modelling tokamak start-up and disruptions. Moving on to optimization, chapter 4 presents what aspects need to be consider when optimizing disruption mitigation. Furthermore, the optimization strategy used in this work, namely Bayesian optimization, is described and its principal components are introduced. Finally, the appended papers are summarized in chapter 5, where we highlight the main results and consider possible areas of future research.

Chapter 2

Runaway electron generation

Electrons with high enough energies are continually accelerated in the presence of a sufficiently strong electric field, as noted by by C. T. R Wilson in 1925 when studying electrons in thunderclouds [20]. The phenomenon was named electron runaway by A. S Eddington in 1926 [21]. Runaway electrons can occur in many other circumstances, such as in solar flares [22] and in tokamak discharges [16]. Regarding the latter, runaway electrons have been detected since the very first tokamak experiments. In reactor-scale devices, runaway electrons are expected to be generated during start-up and disruptions.

There are two specific electric field strength values, the Dreicer field and the critical electric field, that are of particular importance for the dynamics of runaway electrons. The Dreicer field describes the field strength needed for electrons with $v_\parallel \sim v_{\mathrm{th}}$ – that is, the entire electron distribution – to run away (see the top line of figure 2.1) [23], and is given by

$$E_{\mathrm{D}} = \frac{e^3 n_{\mathrm{e}} \ln\Lambda}{4\pi\epsilon_0^2 T_{\mathrm{e}}} = \frac{e^3 n_{\mathrm{e}} \ln\Lambda}{2\pi\epsilon_0^2 m_{\mathrm{e}} v_{\mathrm{th}}^2}, \tag{2.1}$$

where n_{e} is the electron density, and $\ln\Lambda$ is the Coulomb logarithm quantifying the maximum impact parameter of Coulomb collisions [6]. More specifically, all electrons run away if $E_\parallel > 0.2E_{\mathrm{D}}$.

On the other hand, the critical electric field

$$E_{\mathrm{c}} = \frac{e^3 n_{\mathrm{e}} \ln\Lambda}{4\pi\epsilon_0^2 m_{\mathrm{e}} c^2} = \frac{T_{\mathrm{e}}}{m_{\mathrm{e}} c^2} E_{\mathrm{D}} = \frac{v_{\mathrm{th}}^2}{2c^2} E_{\mathrm{D}} \tag{2.2}$$

is the minimum electric field at which runaway electrons can exist (see the bottom line of figure 2.1) – for lower electric fields the collisional forces are always stronger than the Lorentz force. More specifically, equation (2.2) describes the Connor-Hastie field, which is derived by solving the relativistic version of equation (1.7) under the condition that the friction force is minimal [23].

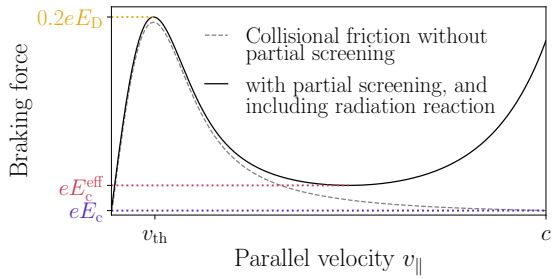

Figure 2.1: Illustration of the decelerating, or braking, force on electrons in a fusion plasma, caused by Coulomb collisions, bremsstrahlung and synchrotron radiation, and including effects from partial screening, as a function of velocity (solid black). The friction force, caused by Coulomb collisions, excluding partial screening effect is illustrated as the dashed gray curve. For all electrons to run away, the electric field $E_\parallel > 0.2E_D$ (dotted yellow). When only the friction force excluding partial screening is considered, runaway electrons can exist above $E_\parallel = E_c$ (dotted purple). If radiation and partial screening is also accounted for, runaway electrons can exist above $E_\parallel = E_c^{eff}$ (dotted red). Note that this figure illustrates the qualitative behaviour of these forces, while the scales and rate of change have been exaggerated.

The expression (2.2) does not account for radiation effects or partial screening, however. Partial screening is an effect connected to electron-ion interactions in partially ionized plasmas. Fast electrons can penetrate the electron cloud of the ion, and experience the ion as having a larger charge than the net charge number – the charge of the ion nucleus is only partially screened by the electron cloud. Bremsstrahlung and synchrotron radiation, as well as partial screening effects, cause the decelerating force to increase for higher velocities, as illustrated in figure 2.1. If these effects are considered, the effective critical electric field E_c^{eff} instead represents the minimum electric field at which runaway electrons can exist [24], which is illustrated as the middle line of figure 2.1.

The electric field is the driving force behind the runaway phenomenon, but the generation of electrons which may run away can be caused by a number of different mechanisms. In this chapter, we present the different generation mechanisms relevant for fusion plasmas. The generation mechanisms can be divided into two categories – primary and secondary generation – based on whether the generation itself is dependent on the existence of runaways in the plasma. Primary generation can occur if the electric field is strong enough, and relevant primary generation mechanisms are Dreicer (see section 2.1) and hot-tail (see section 2.2) generation, as well as generation from tritium beta decay (see section 2.3) and Compton scattering (see section 2.4). If there are already runaway electrons in the plasma, these can generate even more runaway electrons through secondary generation, or more specifically, through avalanche generation (see section 2.5), leading to an exponential increase in the number

of runaway electrons. Primary generation is also commonly known as seed generation, as it provides a seed of runaways that can initialize the substantial growth of the runaway electron population through secondary generation.

2.1 Dreicer generation

In a plasma, thermal electrons are constantly colliding with each other, redistributing their kinetic energy. These collisions act to maintain the electron distribution at the thermal equilibrium, and if any "gaps" would appear in the distribution, they would soon be filled through collisional diffusion. However, as soon as the velocity of an electron is larger than the critical velocity (defined in equation (1.8)), it runs away and is no longer part of the thermal bulk. This leads to a continuous diffusive leak of electrons into the runaway region, and this type of runaway electron generation is called *Dreicer* generation.

The most accurate analytical formula for the Dreicer generation rate was derived by J. Connor and R. Hastie [23]. It was derived by solving the relativistic Fokker-Planck equation using asymptotic techniques in the small parameter E/E_D, neglecting radiation effects and assuming that the plasma is fully ionized. The generation rate is then obtained as

$$\left(\frac{\partial n_\mathrm{re}}{\partial t}\right)_\mathrm{D} = C\frac{n_\mathrm{e}}{\tau_\mathrm{ee}}\left(\frac{E_\parallel}{E_\mathrm{D}}\right)^{-\frac{3}{16}(1+Z_\mathrm{eff})h}\exp\left[-\frac{\lambda}{4}\frac{E_\mathrm{D}}{E_\parallel}-\sqrt{\eta(1+Z_\mathrm{eff})\frac{E_\mathrm{D}}{E_\parallel}}\right], \tag{2.3a}$$

$$\lambda = 8\left(\frac{E_\parallel}{E_\mathrm{c}}\right)^2\left[1-\frac{1}{2}\frac{E_\mathrm{c}}{E_\parallel}-\sqrt{1-\frac{E_\mathrm{c}}{E_\parallel}}\right], \tag{2.3b}$$

$$\eta = \frac{1}{4}\frac{E_\parallel}{E_\mathrm{c}}\frac{1}{1-E_\mathrm{c}/E_\parallel}\left[\frac{\pi}{2}-\arcsin\left(1-2\frac{E_\mathrm{c}}{E_\parallel}\right)\right]^2, \tag{2.3c}$$

$$h = \frac{1}{3}\frac{1}{(E_\parallel/E_\mathrm{c})-1}\left[\frac{E_\parallel}{E_\mathrm{c}}+2\left(\frac{E_\parallel}{E_\mathrm{c}}-2\right)\sqrt{\frac{1}{1-E_\mathrm{c}/E_\parallel}}-\frac{Z_\mathrm{eff}-7}{Z_\mathrm{eff}+1}\right]. \tag{2.3d}$$

Here, the C is an order-unity parameter [25] and the thermal electron collision time is

$$\tau_\mathrm{ee} = \frac{4\pi\epsilon_0^2 m_\mathrm{e}^2 v_\mathrm{th}^3}{n_\mathrm{e} e^4 \ln\Lambda}, \tag{2.4}$$

while the relativistic effects are included through the parameters λ, η and h, which all tend to unity as $E_\parallel/E_\mathrm{c}\to\infty$.

Notably, the Dreicer generation rate is monotonically increasing with, and it is very sensitive to, the electric field, especially for low values of $E_\parallel/E_\mathrm{D}$, as $\gamma_\mathrm{D}\propto\exp\left(-\lambda E_\mathrm{D}/4E_\parallel\right)$. Thus, if $E_\parallel/E_\mathrm{D}$ can be maintained at a relatively low value, significant Dreicer generation can be avoided, regardless of $E_\parallel/E_\mathrm{c}$, at least on relatively short time scales. However, it is worth noting that the expression (2.3) is not necessarily accurate in multi-component plasmas, especially if the assumption of a fully ionized plasma is not valid [26, 27].

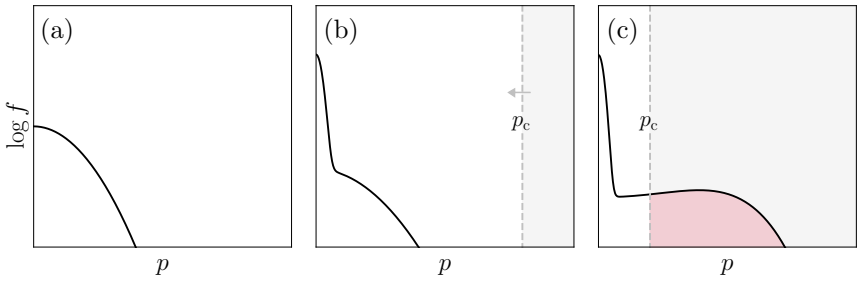

Figure 2.2: Illustration of the hot-tail generation mechanism. (a) Initially, the plasma is in thermal equilibrium, such that the electrons are described by a Maxwellian distribution. (b) As the plasma cools, the distribution develops a hot tail of fast electrons, which cool down slower than slow electrons due to their low collisionality. Simultaneously, the electric field increases rapidly, causing the critical momentum to decrease. (c) The hot tail runs away as the critical momentum becomes sufficiently low.

2.2 Hot-tail generation

During rapid plasma cooling, fast electrons decelerate more slowly than slow electrons, due to their lower collisionality. This results in the distribution function being extended at higher momenta in a tail-like formation [28], which is why this part of the electron population is often referred to as a hot tail – see figure 2.2. If the electric field is rapidly increased, the critical momentum, i.e. the lowest momentum required for an electron to run away, can be reduced to values below this hot tail. Thus, parts of the hot tail can run away, which is referred to as the hot-tail generation mechanism [29, 30].

As the mechanism driving hot-tail generation is the evolution of the distribution function in a cooling plasma, an analytic expression used to estimate the generation rate requires an estimation of the distribution function. Following the derivation in Ref. [31], if source and sink terms, inhomogeneous spatial effects and spatial transport are neglected, the kinetic equation can be formulated as

$$\begin{aligned}\frac{\partial f}{\partial t} = \frac{1}{p^2}\frac{\partial}{\partial p}\left[p^2\left(-eE_\parallel \xi f + \nu_s p f + m_e T_e \gamma \nu_s \frac{\partial f}{\partial p}\right)\right] \\ + \frac{\partial}{\partial \xi}\left[-\frac{1-\xi^2}{p} eE_\parallel f + \left(1-\xi^2\right)\frac{\nu_D}{2}\frac{\partial f}{\partial \xi}\right].\end{aligned} \tag{2.5}$$

Here, T_e is the electron temperature, and ν_D and ν_s are the pitch angle scattering and slowing down collision frequencies, respectively. This kinetic equation is described in terms of the magnitude of the momentum $p = |\boldsymbol{p}|$, with the Lorentz factor $\gamma = \sqrt{p^2+1}$, and the pitch $\xi = \boldsymbol{p}\cdot\boldsymbol{B}/(pB)$. Using

$$\frac{1}{p^2}\frac{\partial\left(p^2\xi f\right)}{\partial p} = \frac{2\xi}{p}f + \xi\frac{\partial f}{\partial p} \quad \text{and} \quad \frac{\partial}{\partial \xi}\left(\frac{1-\xi^2}{p}f\right) = -\frac{2\xi}{p}f + \frac{1-\xi^2}{p}\frac{\partial f}{\partial \xi}, \tag{2.6}$$

this can be simplified to

$$\frac{\partial f}{\partial t} = -eE_\parallel \left[\xi \frac{\partial f}{\partial p} + \frac{1-\xi^2}{p}\frac{\partial f}{\partial \xi}\right] + \frac{1}{p^2}\frac{\partial}{\partial p}\left[\nu_\mathrm{s} p^3 f + m_\mathrm{e} T_\mathrm{e} p^2 \gamma \nu_\mathrm{s} \frac{\partial f}{\partial p}\right] + \frac{\nu_\mathrm{D}}{2}\frac{\partial}{\partial \xi}\left[\left(1-\xi^2\right)\frac{\partial f}{\partial \xi}\right]. \tag{2.7}$$

We introduce the (small) ordering parameter δ, defined such that that the pitch angle collision frequency $\nu_\mathrm{D} \sim \delta^0$, which is valid during strong pitch angle scattering. For $T_\mathrm{e} \ll m_\mathrm{e}c^2 \approx 511\,\mathrm{keV}$, the energy diffusion term, namely the term with diffusion coefficient $D \propto T_\mathrm{e}\nu_\mathrm{s}$, is negligible and can be ordered as $\lesssim \delta^2$, while all other terms can be ordered as $\sim \delta$. Furthermore, the distribution expanded with regard to this ordering parameter, i.e. $f = f_0 + \delta f_1 + \mathcal{O}(\delta^2)$, yields the kinetic equation

$$\frac{\partial f_0}{\partial t} = -eE_\parallel \left[\xi \frac{\partial f_0}{\partial p} + \frac{1-\xi^2}{p}\frac{\partial f_0}{\partial \xi}\right] + \frac{1}{p^2}\frac{\partial}{\partial p}\left[\nu_\mathrm{s} p^3 f_0\right] + \frac{\nu_\mathrm{D}}{2}\frac{\partial}{\partial \xi}\left[\left(1-\xi^2\right)\left(\frac{\partial f_0}{\partial \xi} + \delta\frac{\partial f_1}{\partial \xi}\right)\right] + \mathcal{O}(\delta^2). \tag{2.8}$$

The kinetic equation (2.8) can now be separated with regard to order

$$\delta^0 : \; 0 = \frac{\nu_\mathrm{D}}{2}\frac{\partial}{\partial \xi}\left[\left(1-\xi^2\right)\frac{\partial f_0}{\partial \xi}\right], \tag{2.9a}$$

$$\delta^1 : \; \frac{\partial f_0}{\partial t} = -eE_\parallel \left[\xi \frac{\partial f_0}{\partial p} + \frac{1-\xi^2}{p}\frac{\partial f_0}{\partial \xi}\right] + \frac{1}{p^2}\frac{\partial}{\partial p}\left[\nu_\mathrm{s} p^3 f_0\right] + \frac{\nu_\mathrm{D}}{2}\frac{\partial}{\partial \xi}\left[\left(1-\xi^2\right)\frac{\partial f_1}{\partial \xi}\right]. \tag{2.9b}$$

Equation (2.9a) implies that the first order term of the distribution function is isotropic in pitch-angle, i.e. $\partial f_0/\partial \xi = 0$, which when inserted into equation (2.9b) yields

$$\frac{\partial f_0}{\partial t} = -eE_\parallel \xi \frac{\partial f_0}{\partial p} + \frac{1}{p^2}\frac{\partial}{\partial p}\left[\nu_\mathrm{s} p^3 f_0\right] + \frac{\nu_\mathrm{D}}{2}\frac{\partial}{\partial \xi}\left[\left(1-\xi^2\right)\frac{\partial f_1}{\partial \xi}\right]. \tag{2.10}$$

Since we are interested in f_0, which is independent of pitch angle, we can average our kinetic equation over pitch-angle,

$$\frac{1}{2}\int_{-1}^{1} \frac{\partial f_0}{\partial t}\mathrm{d}\xi = \frac{\partial f_0}{\partial t}, \tag{2.11a}$$

$$\frac{1}{2}\int_{-1}^{1} eE_\parallel \xi \frac{\partial f_0}{\partial p}\mathrm{d}\xi = 0, \tag{2.11b}$$

$$\frac{1}{2}\int_{-1}^{1} \frac{1}{p^2}\frac{\partial}{\partial p}\left[\nu_\mathrm{s} p^3 f_0\right]\mathrm{d}\xi = \frac{1}{p^2}\frac{\partial}{\partial p}\left[\nu_\mathrm{s} p^3 f_0\right], \tag{2.11c}$$

$$\frac{1}{2}\int_{-1}^{1} \frac{\nu_\mathrm{D}}{2}\frac{\partial}{\partial \xi}\left[\left(1-\xi^2\right)\delta\frac{\partial f_1}{\partial \xi}\right]\mathrm{d}\xi = 0, \tag{2.11d}$$

resulting in the reduced kinetic equation

$$\frac{\partial f_0}{\partial t} = \frac{1}{p^2}\frac{\partial}{\partial p}\left[\nu_\mathrm{s} p^3 f_0\right]. \tag{2.12}$$

In order to solve this reduced kinetic equation, we introduce the electron collision time

$$\tau_\mathrm{c} = \frac{4\pi\epsilon_0^2 m_\mathrm{e}^2 c^3}{n_\mathrm{e} e^4 \ln\Lambda}. \tag{2.13}$$

Furthermore, the slowing down collision frequency can be expressed as [32]

$$\nu_\mathrm{s} = \frac{1}{\tau_\mathrm{c}}\frac{\gamma^2}{p^3}, \tag{2.14}$$

which when inserted into the kinetic equation (2.12) yields

$$\frac{\partial f_0}{\partial t} = \frac{1}{\tau_\mathrm{c}}\frac{1}{p^2}\frac{\partial}{\partial p}\left[\gamma^2 f_0\right]. \tag{2.15}$$

Assuming that τ_c varies slowly in time, such that the time dependence can be neglected, and taking the non-relativistic limit (i.e. $\gamma = 1$), the general solution to equation (2.15) is

$$f_0 = \frac{1}{\gamma^2}G(s) = G(s), \tag{2.16}$$

for some function $G(s)$, with

$$\begin{aligned} s(t,p) &= \int_0^p \left(\frac{p'}{\gamma'}\right)^2 \mathrm{d}p' + \int_0^t \frac{\mathrm{d}t'}{\tau_\mathrm{c}} \\ &= \int_0^p \left(p'\right)^2 \mathrm{d}p' + \int_0^t \frac{\mathrm{d}t'}{\tau_\mathrm{c}} \\ &= \frac{p^3}{3} + \int_0^t \frac{\mathrm{d}t'}{\tau_\mathrm{c}}. \end{aligned} \tag{2.17}$$

Initially, the plasma should be in thermal equilibrium, meaning that

$$G(s)\Big|_{t=0} = \frac{n_\mathrm{e}}{\pi^{3/2} p_{\mathrm{th},0}^2}\exp\left(-\frac{p^2}{p_{\mathrm{th},0}^2}\right) \tag{2.18a}$$

$$\implies G(s) = \frac{n_\mathrm{e}}{\pi^{3/2} p_{\mathrm{th},0}^2}\exp\left(-\frac{(3s)^{2/3}}{p_{\mathrm{th},0}^2}\right), \tag{2.18b}$$

where $p_{\mathrm{th},0} = \sqrt{2T_{\mathrm{e}0}/m_\mathrm{e}c^2}$ is the initial thermal momentum normalized to $m_\mathrm{e}c$. This yields the final solution

$$f_0(t,p) = \frac{n_\mathrm{e}}{\pi^{3/2} p_{\mathrm{th},0}^3}\exp\left(-\frac{\left[p^3 + 3\tau(t)\right]^{2/3}}{p_{\mathrm{th},0}^2}\right), \tag{2.19a}$$

$$\tau(t) = \int_0^t \frac{\mathrm{d}t'}{\tau_\mathrm{c}}. \tag{2.19b}$$

As the runaway electron density is defined by the distribution function moment according to

$$n_{\mathrm{re}} = \int_{p_{\mathrm{c}}(t)}^{\infty} f(t, \boldsymbol{p}) \mathrm{d}^3\boldsymbol{p}, \tag{2.20}$$

the hot-tail generation rate can be obtained by differentiating this with regard to time. Given the analytical expression for the leading order term of the distribution function derived above, which is isotropic with regard to pitch angle, we can simplify the evaluation of the generation rate. Importantly, the assumption of strong pitch angle scattering is typically valid for electrons with velocities below the critical velocity, as for these electrons, the collisions dominate the dynamics over the effect of the electric field.

The critical momentum $p_{\mathrm{c}} \approx \sqrt{E_{\mathrm{c}}/E_{\parallel}}$ is here defined from the kinetic equation as the momentum at which the electric field acceleration terms and collisional friction are equal, and is thus a time dependent parameter. Assuming that the effect of the electric field, while being a weaker effect than pitch angle scattering (as we did in equation (2.9)), is stronger than remaining effects, it can be included in the kinetic equation (2.15) as a diffusion term. The resulting expression is derived in more detail in section 3.1, but with radial transport. Thus, under these assumptions, the kinetic equation can be formulated as

$$\frac{\partial f_0}{\partial t} = \frac{1}{p^2}\frac{\partial}{\partial p}\left[p^2\left(-A^p f_0 + D^{pp}\frac{\partial f_0}{\partial p}\right)\right] \tag{2.21}$$

instead. The critical momentum p_{c} is then defined as

$$-A^p f_0 + D^{pp}\frac{\partial f_0}{\partial p}\bigg|_{p=p_{\mathrm{c}}} = 0. \tag{2.22}$$

Using the leading order term of the distribution function f_0, the hot-tail generation rate can be estimated from

$$n_{\mathrm{re}} = 4\pi \int_{p_{\mathrm{c}}(t)}^{\infty} p^2 f_0(t, \boldsymbol{p}) \mathrm{d}p \tag{2.23a}$$

$$\implies \frac{\partial n_{\mathrm{re}}}{\partial t} = -4\pi p_{\mathrm{c}}^2 \frac{\partial p_{\mathrm{c}}}{\partial t} f_0(t, p_{\mathrm{c}}) + 4\pi \int_{p_{\mathrm{c}}}^{\infty} p^2 \frac{\partial f_0}{\partial t}\mathrm{d}p, \tag{2.23b}$$

where p_{c} can be evaluated from solving equation (2.22). The second term on the right hand side of this expression is equal to zero, as

$$\begin{aligned}
\int_{p_{\mathrm{c}}}^{\infty} p^2 \frac{\partial f_0}{\partial t}\mathrm{d}p &= \int_{p_{\mathrm{c}}}^{\infty} \frac{\partial}{\partial p}\left[p^2\left(-A^p f_0 + D^{pp}\frac{\partial f_0}{\partial p}\right)\right]\mathrm{d}p \\
&= \left[p^2\left(-A^p f_0 + D^{pp}\frac{\partial f_0}{\partial p}\right)\right]_{p_{\mathrm{c}}}^{\infty} \\
&= p_{\mathrm{c}}^2\left(-A^p f_0 + D^{pp}\frac{\partial f_0}{\partial p}\right)\bigg|_{p_{\mathrm{c}}} \\
&= 0.
\end{aligned} \tag{2.24}$$

Thus, the hot-tail generation rate is obtained as

$$\left(\frac{\partial n_{\mathrm{re}}}{\partial t}\right)_{\mathrm{ht}} = -4\pi p_{\mathrm{c}}^2 \frac{\partial p_{\mathrm{c}}}{\partial t} f_0(t, p_{\mathrm{c}}), \tag{2.25a}$$

$$f_0(t,p) = \frac{n_{\mathrm{e}}}{\pi^{3/2} p_{\mathrm{th},0}^3} \exp\left(-\frac{\left[p^3 + 3\int_0^t (1/\tau_{\mathrm{c}})\,\mathrm{d}t'\right]^{2/3}}{p_{\mathrm{th},0}^2}\right). \tag{2.25b}$$

This is recognized as the hot-tail generation rate since the driving mechanism of this generation rate is the varying critical momentum, in accordance with the hot-tail mechanism, and not collisional diffusion as for Dreicer generation.

2.3 Tritium beta decay

Tritium is a radioactive isotope with a half-life of 12 years, which decays through beta-decay according to

$$\mathrm{T} \rightarrow {}^3_2\mathrm{He} + \bar{\nu}_{\mathrm{e}} + \mathrm{e}^-. \tag{2.26}$$

If this reaction occurs in a plasma, the electron runs away if it is emitted with a velocity greater than the critical velocity. Generation of runaway electrons from tritium beta decay will be relevant in fusion reactors, as tritium will be used as fuel due to its relatively high cross section for fusion with deuterium.

During tritium beta decay, the emission of electrons follows the energy spectrum described by [33]

$$f_\beta(W) \propto \begin{cases} F(p,2)p\mathcal{W}(W_{\max} - W)^2 & \text{for } W \leq W_{\max}, \\ 0 & \text{for } W \geq W_{\max}, \end{cases} \tag{2.27a}$$

$$\int_0^\infty f_\beta(W)\mathrm{d}W = 1, \tag{2.27b}$$

with the momentum p normalized to $m_{\mathrm{e}}c$, Lorentz factor $\gamma = \sqrt{p^2+1}$, kinetic energy $W = m_{\mathrm{e}}c^2(\gamma - 1)$ and total energy $\mathcal{W} = m_{\mathrm{e}}c^2\gamma$. The maximum kinetic energy possible for an electron to be emitted with is $W_{\max} = 18.6\,\mathrm{keV}$. In equation (2.27a), $F(p,\, Z_{\mathrm{f}})$ is the Fermi function [34]. As $W_{\max} \ll m_{\mathrm{e}}c^2$, the non-relativistic limit of the Fermi function can be used for describing the energy spectrum of the tritium beta decay (2.27a), which is

$$F(p,\, Z_{\mathrm{f}}) = \frac{2\pi\alpha Z_{\mathrm{f}}\gamma/p}{1 - \exp\left(-2\pi\alpha Z_{\mathrm{f}}\gamma/p\right)}, \tag{2.28}$$

where Z_{f} is the charge of the final state nucleus and $\alpha \approx 1/137$ is the fine structure constant. The beta decay energy spectrum is plotted in figure 2.3.

Given the critical kinetic energy for runaway generation W_{c}, the runaway generation rate from tritium beta decay is described by [35, 36],

$$\left(\frac{\partial n_{\mathrm{re}}}{\partial t}\right)_{\mathrm{T}} \approx \ln 2 \frac{n_{\mathrm{T}}}{\tau_{\mathrm{T}}} \int_{W_{\mathrm{c}}}^{W_{\max}} f_\beta(W)\mathrm{d}W. \tag{2.29}$$

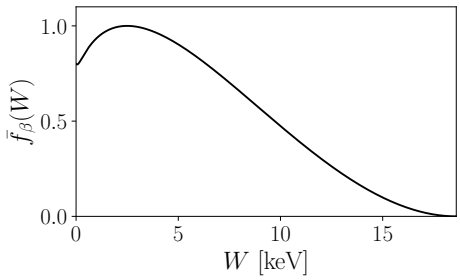

Figure 2.3: The normalized energy spectrum of electrons emitted during beta decay $\bar{f}_\beta(W)$ as a function of kinetic energy W, normalized so that $\max \bar{f}_\beta = 1$.

Notably, if $W_\mathrm{c} = 0$ could be achieved, the generation of runaway electrons would be equal to the total generation rate of electrons from the decay, i.e. $\ln 2 \cdot n_\mathrm{T}/\tau_\mathrm{T}$ which depends on the tritium density n_T and half-life $\tau_\mathrm{T} \approx 4500\,\mathrm{days}$.

2.4 Compton scattering

Photons can interact with electrons through Compton scattering, during which the electrons can obtain a fraction of the photon energy and attain a significantly higher speed. This Compton effect can generate runaway electrons in a plasma, and can occur in a fusion reactor due to photons emitted by the activated walls when operating a deuterium-tritium plasma. During the fusion of deuterium and tritium,

$$\mathrm{D} + \mathrm{T} \rightarrow \alpha + \mathrm{n}, \tag{2.30}$$

neutrons are emitted, and the neutron bombardment of the fusion reactor wall causes the wall material to become radioactive. When the radioactive wall material decays, γ-photons are emitted, which can scatter off both free and bound electrons in the plasma, and potentially cause them to run away.

The differential cross-section for Compton scattering is given by the Klein-Nishina formula [37]

$$\frac{\mathrm{d}\sigma}{\mathrm{d}\Omega} = \frac{r_\mathrm{e}^2}{2}\frac{W_\gamma'^2}{W_\gamma^2}\left[\frac{W_\gamma}{W_\gamma'} + \frac{W_\gamma'}{W_\gamma} - \sin^2(\theta)\right], \tag{2.31}$$

where W_γ is the initial and W_γ' the scattered photon energy, θ is the deflection angle of the scattered photon, and $r_\mathrm{e} = e^2/4\pi\epsilon_0 m_\mathrm{e} c^2$ is the classical electron radius. The photon energies and the deflection angle are related by

$$\cos\theta = 1 - \frac{m_\mathrm{e}c^2}{W_\gamma}\frac{W}{W_\gamma'}, \tag{2.32}$$

under the assumption that the initial electron kinetic energy is negligible compared to the initial photon energy. The electron energy W after the

scattering event W can be obtained through energy conservation, i.e. $W_\gamma = W'_\gamma + W$.

Given a photon energy spectrum $\Gamma_\gamma(W_\gamma)$ and critical kinetic energy W_c for electrons to run away, the generation rate of runaway electrons from Compton scattering is obtained as [35, 36]

$$\left(\frac{\partial n_\mathrm{re}}{\partial t}\right)_\mathrm{C} \approx n_\mathrm{e,tot} \int \Gamma_\gamma(W_\gamma) \int_{\theta_\mathrm{c}}^{\pi} \frac{\mathrm{d}\sigma}{\mathrm{d}\Omega}\,\mathrm{d}\Omega\,\mathrm{d}W_\gamma. \tag{2.33}$$

Here, $\theta_\mathrm{c} = \theta(W_\mathrm{c}, W_\gamma)$ is the critical deflection angle for electrons to run away and $n_\mathrm{e,tot}$ is the total number density of electrons available for photons to scatter on.

2.5 Avalanche generation

If there exists a seed of runaway electrons in the plasma, more runaways can be generated through collisions with other electrons. When a runaway electron collides with a slow electron, a part of its kinetic energy is transferred, and this can result in them both having a velocity above the critical velocity after the collision. At this point, both of the electrons are continually accelerated. This mechanism is called avalanche generation, as it can lead to an exponential increase in the number of runaway electrons [19, 25, 38].

The generation from avalanche multiplication is described by

$$\left(\frac{\partial n_\mathrm{re}}{\partial t}\right)_\mathrm{ava} = \Gamma_\mathrm{ava} n_\mathrm{re}, \tag{2.34}$$

where Γ_ava is the avalanche growth rate, which depends on the electric field strength $E_\parallel$. For plasmas with $E_\parallel \gg E_\mathrm{c}$, the avalanche multiplication should be strong, and more specifically the growth rate should be approximately proportional to $E_\parallel$. On the other hand, the avalanche multiplication should vanish as $E_\parallel \to E_\mathrm{c}^\mathrm{eff}$. If partial screening is accounted for, the avalanche growth rate can be described by [38]

$$\Gamma_\mathrm{ava} = \frac{e}{m_\mathrm{e} c \ln\Lambda_\mathrm{c}} \frac{n_\mathrm{e,tot}}{n_\mathrm{th}} \frac{E_\parallel - E_\mathrm{c}^\mathrm{eff}}{\sqrt{4 + \bar{\nu}_s(p_\mathrm{c}^\star)\bar{\nu}_D(p_\mathrm{c}^\star)}}. \tag{2.35}$$

Here, n_th is the density of free, thermal electrons, $\ln\Lambda_\mathrm{c}$ is the relativistic Coulomb logarithm, and the normalized collision frequencies $\bar{\nu}_\mathrm{s}$ and $\bar{\nu}_\mathrm{D}$ have been derived to account for partial screening effects. Furthermore, $p_\mathrm{c}^\star$ is an effective critical momentum for runaway generation defined in Ref. [38] as

$$p_\mathrm{c}^{\star 2} = \frac{\sqrt{\bar{\nu}_s(p_\mathrm{c}^\star)\bar{\nu}_D(p_\mathrm{c}^\star)}}{E_\parallel/E_\mathrm{c}}. \tag{2.36}$$

Notably, for avalanche generation to occur, the conditions for any of the primary generation mechanisms need to be fulfilled. However, if there is a large enough seed population (note that large enough does not necessarily mean large), the avalanche generation typically dominates runaway generation, despite the low collisionality of runaway electrons.

Chapter 3

Start-up and disruption modelling

There are currently several large devices under construction (such as SPARC and ITER) where significant runaway electron generation is expected and could be devastating. It is necessary to develop viable strategies of operation, using a combination of both numerical and physical experiments. Numerical experiments enable a wider exploration of operational regimes, and can help in predicting how results of existing physical experiments will extrapolate to future, larger machines. When designing a numerical model for tokamak plasmas, it must account for electromagnetic forces, inter-particle interactions and inelastic atomic processes. In this chapter we summarize the plasma models used in papers A, B, C and D.

The key elements modelled are the different particle species, with the corresponding densities and temperatures, as well as the electric field and characteristic current densities, which all need to be evolved in parallel and self-consistently. How these plasma quantities are modelled is described in more detail for tokamak disruptions in section 3.1 and for start-up in section 3.2, but let us here present a summary of important considerations valid for both. For both start-up and disruptions, we consider heating caused by the electric field, i.e. Ohmic heating, and collisional heat transfer between particle species, as well as energy losses due to inelastic atomic processes in evolving the temperatures. Regarding the electric field and the total plasma current, they are modelled based on Faraday's, Ampère's and Ohm's laws for both start-up and disruptions.

Additionally, since the main focus of the aforementioned studies is the generation and dynamics of runaway electrons, the electron modelling is here given particular consideration. For numerical convenience, we divide the electrons into three distinct populations based on their momentum – thermal, or cold, electrons at relatively low momenta; superthermal, or hot, electrons at moderate momenta; and runaway electrons at momenta significantly above the critical momentum. Thermal electrons make up the bulk of the plasma,

and are defined to be described by a Maxwellian distribution. The thermal electron density is evolved to ensure quasineutrality in the plasma. Notably, the superthermal population is only distinguished from the thermal population for kinetic modelling, as the purpose of defining the superthermal population is to describe the dynamics near the critical momentum kinetically.

In the papers A, B, C and D, the runaway electrons have been modelled as a fluid, characterized only by their density. From the density, the current density can be approximated as $j_{\mathrm{re}} = n_{\mathrm{re}} ec$ [39], as the runaway electrons travel close to the speed of light, dominantly parallel to the field lines. This assumption is typically valid in reactor-scale tokamak disruptions, and sets an upper limit for the runaway current magnitude. The runaway density is determined by source terms representing the different generation mechanisms, as well as a sink term representing particle transport. For both start-up and disruptions, avalanche generation is expected to dominate the generation when a runaway seed has been formed, and for start-up the main seed generation mechanism that needs to be considered is Dreicer generation, due to the low prefill pressures associated with start-up. During disruptions, we additionally need to consider runaway electron seed generation from tritium beta decay and Compton scattering, as well as from the hot-tail generation phenomenon present during plasma cooling.

The models for tokamak start-up and disruptions presented here are similar, but notably, the disruption model is of higher dimensionality. More specifically, it considers both the radial dependence of the plasma and resolves dynamics in momentum space. In the start-up model, the system of equations governing the electric field and current evolution can be obtained from reducing the disruption plasma model to 0D. Furthermore, the equations for evolving the plasma temperatures and densities in the start-up model can be obtained by expanding the disruption model to include neutral screening effects. For these reasons, the disruption model is presented before the start-up model.

3.1 Modelling disruptions

The plasma model used for disruption simulations in this thesis reduces the computational complexity by only retaining one spatial dimension, and up to one dimension in momentum space [40]. More specifically, only the superthermal electrons are modelled kinetically, with a distribution function which has been analytically averaged over pitch angle. Spatially, we assume that the plasma composition is homogeneous on each flux surface, and the dynamics of the plasma is only modelled along the minor radius r.

In reality, the dynamics in a tokamak are not poloidally symmetric, especially since the toroidal magnetic field varies as $1/R$. The total magnetic field can be modelled by the magnetic poloidal flux $\psi(r) = 2\pi \int_0^{R(r)} (\boldsymbol{B} \cdot \hat{Z})\, R \,\mathrm{d}R$ together with a toroidal magnetic field function $G(r)$, which describes the spatial dependence of the magnetic field, according to

$$\boldsymbol{B}(r,\theta) = G(r)\nabla\varphi + \frac{1}{2\pi}\nabla\varphi \times \nabla\psi(r), \tag{3.1}$$

where φ is the toroidal angle and θ the poloidal angle. To approximately account for the effect of the poloidal dependence of the magnetic field on the dynamics, the plasma quantities are flux surface averaged. The flux surface average of a quantity X is defined as

$$\langle X \rangle = \frac{1}{V'} \int_0^{2\pi} \int_{-\pi}^{\pi} X \mathcal{J} \, \mathrm{d}\theta \, \mathrm{d}\varphi, \tag{3.2}$$

with

$$V' = \int_0^{2\pi} \int_{-\pi}^{\pi} \mathcal{J} \, \mathrm{d}\theta \, \mathrm{d}\varphi, \tag{3.3}$$

$$\mathcal{J} = \frac{1}{|\nabla\varphi \cdot (\nabla\theta \times \nabla r)|}, \tag{3.4}$$

where the flux surface geometry is accounted for in the spatial Jacobian $\mathcal{J}$, i.e. the elongation, triangularity and Shafranov shift.

Electric field and currents

The evolution of the electric field and plasma current is governed by the poloidal magnetic flux. The electric field $\boldsymbol{E}$ is determined by the poloidal flux $\psi(r)$ through the loop voltage U in the plasma, as according to Faraday's law

$$\frac{\partial \psi}{\partial t} = U, \tag{3.5}$$

and the loop voltage is related to the electric field through

$$U = 2\pi \frac{\langle \boldsymbol{E} \cdot \boldsymbol{B} \rangle}{\langle \boldsymbol{B} \cdot \nabla\varphi \rangle}. \tag{3.6}$$

At the wall ($r = b$), the loop voltage and poloidal flux are determined by the wall resistivity and external inductance, forming the boundary conditions

$$U_{\mathrm{wall}} = R_{\mathrm{wall}} I_{\mathrm{wall}}, \tag{3.7a}$$

$$\psi_{\mathrm{wall}} = -L_{\mathrm{ext}}(I_{\mathrm{p}} + I_{\mathrm{wall}}). \tag{3.7b}$$

Here, the external inductance is assumed to be $L_{\mathrm{ext}} = \mu_0 R_0 \ln(R_0/b)$, which, together with the characteristic wall time τ_{wall}, determines the wall resistivity $R_{\mathrm{wall}} = L_{\mathrm{ext}}/\tau_{\mathrm{wall}}$.

For the plasma current, the poloidal flux and the total parallel plasma current density j_{tot} satisfy Ampère's law

$$2\pi\mu_0 \langle \boldsymbol{B} \cdot \nabla\varphi \rangle \frac{j_{\mathrm{tot}}}{B} = \frac{1}{V'} \frac{\partial}{\partial r} \left[V' \left\langle \frac{|\nabla r|^2}{R^2} \right\rangle \frac{\partial \psi}{\partial r} \right], \tag{3.8}$$

and the total plasma current I_{p} is obtained by integrating the total parallel current density over the poloidal cross section

$$I_{\mathrm{p}} = \frac{1}{2\pi} \int_0^a V' \langle \boldsymbol{B} \cdot \nabla\varphi \rangle \frac{j_{\mathrm{tot}}}{B} \mathrm{d}r. \tag{3.9}$$

The total current density can be divided into three components, corresponding to the three electron populations, i.e. $j_{\mathrm{tot}} = j_\Omega + j_{\mathrm{st}} + j_{\mathrm{re}}$. The Ohmic current is coupled to the electric field through Ohm's law

$$j_\Omega = \sigma \frac{\langle \boldsymbol{E} \cdot \boldsymbol{B} \rangle}{\sqrt{\langle B^2 \rangle}}, \tag{3.10}$$

where σ is the parallel electric conductivity [41]. As previously mentioned, the runaway current density is determined by the runaway density n_{re} according to $j_{\mathrm{re}} = n_{\mathrm{re}} ec$. If the superthermal population is modelled, its current density j_{st} is evaluated as a moment of the superthermal distribution function.

Reduced kinetic equation

The main purpose of distinguishing the superthermal population from the thermal population, and modelling it kinetically, is to obtain a more accurate description of the runaway electron seed generation. The momentum range in which the superthermal population is defined should therefore encompass the typical values of the critical momentum p_{c} for runaway electron generation, as the seed generation dynamics occur mostly around $p \sim p_{\mathrm{c}}$. The dynamics at momenta below the critical momentum is often dominated by pitch-angle scattering during disruptions. Under the assumption of dominating pitch angle scattering, it is possible to reduce the complexity of the kinetic model through a perturbative treatment of the dynamics with the pitch angle scattering time being the small parameter.

The full kinetic equation in cylindrical geometry for the superthermal electrons during a disruption is [40]

$$\begin{aligned} \frac{\partial f}{\partial t} = {} & \frac{1}{p^2}\frac{\partial}{\partial p}\left[p^2\left(-\langle A^p\rangle f + \langle D^{pp}\rangle \frac{\partial f}{\partial p}\right)\right] + \frac{\partial}{\partial \xi}\left[-\langle A^\xi\rangle f + \langle D^{\xi\xi}\rangle \frac{\partial f}{\partial \xi}\right] \\ & + \frac{1}{V'}\frac{\partial}{\partial r}\left[V'\left(-\langle A^r\rangle f + \langle D^{rr}\rangle \frac{\partial f}{\partial r}\right)\right] + \langle S\rangle, \end{aligned} \tag{3.11}$$

where the $\langle A\rangle$ terms represent advection, $\langle D\rangle$ terms represent diffusion and $\langle S\rangle$ represent all particle sources to be considered. Note that all of these terms are flux surface averaged (see equation (3.2)), as denoted by $\langle\cdot\rangle$. The two most important effects are pitch angle scattering and electric field acceleration. Pitch angle scattering leads to a diffusive process described by

$$\langle D^{\xi\xi}_{\mathrm{D}} \rangle = \left(1 - \xi^2\right) \frac{\nu_{\mathrm{D}}(p)}{2}, \tag{3.12}$$

where $\nu_{\mathrm{D}}(p)$ is the pitch angle scattering, or deflection, collision frequency, which depends on momentum. The electric field acceleration is modelled through momentum and pitch-angle advection, described by

$$\langle A^p_E \rangle = \xi \frac{e\langle \boldsymbol{E} \cdot \boldsymbol{B} \rangle}{B}, \tag{3.13a}$$

$$\langle A^\xi_E \rangle = \frac{1 - \xi^2}{p} \frac{e\langle \boldsymbol{E} \cdot \boldsymbol{B} \rangle}{B}. \tag{3.13b}$$

The part of the momentum advection that is not due to the electric field is denoted by $\langle \hat{A}^p \rangle = \langle A^p \rangle - \langle A^p_E \rangle$, and it includes slowing down effects due to collisions $\langle A^p_{\mathrm{C}} \rangle = -\nu_{\mathrm{s}} p$, bremsstrahlung $\langle A^p_{\mathrm{B}} \rangle = -\nu^{\mathrm{B}}_{\mathrm{s}} p$ and synchrotron radiation $\langle A^p_{\mathrm{S}} \rangle \propto -p\gamma(1-\xi^2)$. Slowing down effects due to collisions are also included in the momentum space diffusion $\langle D^{pp}_{\mathrm{C}} \rangle = m_{\mathrm{e}} T_{\mathrm{th}} \gamma \nu_{\mathrm{s}}$, where T_{th} is the temperature of the thermal electron population, and due to synchrotron radiation in the pitch angle space advection $\langle A^\xi_{\mathrm{S}} \rangle \propto -\xi(1-\xi^2)/\gamma$. Finally, we account for radial transport effects through $\langle D^{rr} \rangle$ and $\langle A^r \rangle$, which are described in detail later on in this section.

Assuming strong pitch angle scattering, we can introduce the (small) ordering parameter δ such that the pitch angle scattering collision frequency $\nu_{\mathrm{D}} \sim \delta^0$ and the parallel electric field $\langle \boldsymbol{E} \cdot \boldsymbol{B} \rangle / B \sim \delta^1$, while all other terms are $\sim \delta^2$. Furthermore, expanding the distribution function with regard to the ordering parameter, i.e. $f = f_0 + \delta f_1 + \delta^2 f_2 + \mathcal{O}(\delta^3)$, and inserting it into the kinetic equation (3.11) together with (3.12), (3.13a) and (3.13b) yields

$$\begin{aligned}
\frac{\partial f_0}{\partial t} = {} & \frac{1}{p^2}\frac{\partial}{\partial p}\left[p^2\left(-\xi\frac{e\langle \boldsymbol{E}\cdot\boldsymbol{B}\rangle}{B}(f_0+\delta f_1) - \langle \hat{A}^p\rangle f_0 + \langle D^{pp}\rangle \frac{\partial f_0}{\partial p}\right)\right] \\
& + \frac{\partial}{\partial \xi}\left[-\frac{1-\xi^2}{p}\frac{e\langle \boldsymbol{E}\cdot\boldsymbol{B}\rangle}{B}(f_0+\delta f_1) - \langle A^\xi_{\mathrm{S}}\rangle f_0 \right. \\
& \left. + \left(1-\xi^2\right)\frac{\nu_{\mathrm{D}}}{2}\left(\frac{\partial f_0}{\partial \xi} + \delta\frac{\partial f_1}{\partial \xi} + \delta^2\frac{\partial f_2}{\partial \xi}\right)\right] \\
& + \frac{1}{V'}\frac{\partial}{\partial r}\left[V'\left(-\langle A^r\rangle f_0 + \langle D^{rr}\rangle\frac{\partial f_0}{\partial r}\right)\right] \\
& + \langle S\rangle + \mathcal{O}(\delta^3).
\end{aligned} \tag{3.14}$$

We can now separate equation (3.14) into three equations based on their order in δ:

$$\delta^0 : \; 0 = \frac{\nu_{\mathrm{D}}}{2}\frac{\partial}{\partial \xi}\left[\left(1-\xi^2\right)\frac{\partial f_0}{\partial \xi}\right], \tag{3.15a}$$

$$\begin{aligned}
\delta^1 : \; 0 = {} & -\frac{e\langle \boldsymbol{E}\cdot\boldsymbol{B}\rangle}{B}\left[\frac{\xi}{p^2}\frac{\partial\left(p^2 f_0\right)}{\partial p} + \frac{1}{p}\frac{\partial\left(\left(1-\xi^2\right)f_0\right)}{\partial \xi}\right] \\
& + \frac{\nu_{\mathrm{D}}}{2}\frac{\partial}{\partial \xi}\left[\left(1-\xi^2\right)\frac{\partial f_1}{\partial \xi}\right],
\end{aligned} \tag{3.15b}$$

$$\begin{aligned}
\delta^2 : \; \frac{\partial f_0}{\partial t} = {} & -\frac{e\langle \boldsymbol{E}\cdot\boldsymbol{B}\rangle}{B}\left[\frac{\xi}{p^2}\frac{\partial\left(p^2 f_1\right)}{\partial p} + \frac{1}{p}\frac{\partial\left(\left(1-\xi^2\right)f_1\right)}{\partial \xi}\right] \\
& + \frac{\nu_{\mathrm{D}}}{2}\frac{\partial}{\partial \xi}\left[\left(1-\xi^2\right)\frac{\partial f_2}{\partial \xi}\right] + \frac{\partial}{\partial \xi}\left[-\langle A^\xi_{\mathrm{S}}\rangle f_0\right] \\
& + \frac{1}{p^2}\frac{\partial}{\partial p}\left[p^2\left(-\langle \hat{A}^p\rangle f_0 + \langle D^{pp}\rangle\frac{\partial f_0}{\partial p}\right)\right] \\
& + \frac{1}{V'}\frac{\partial}{\partial r}\left[V'\left(-\langle A^r\rangle f_0 + \langle D^{rr}\rangle\frac{\partial f_0}{\partial r}\right)\right] \\
& + \langle S\rangle.
\end{aligned} \tag{3.15c}$$

According to equation (3.15a), $\partial f_0/\partial\xi = 0$ or equivalently $f_0 = f_0(t, r, p)$, meaning that, to the lowest order, the distribution function is isotropic in pitch angle. Using this in equation (3.15b), we get

$$\begin{aligned}\frac{\partial}{\partial\xi}\left[\left(1-\xi^2\right)\frac{\partial f_1}{\partial\xi}\right] &= 2\frac{e\langle\boldsymbol{E}\cdot\boldsymbol{B}\rangle}{\nu_{\mathrm{D}}B}\left[\xi\frac{\partial f_0}{\partial p}+\frac{2\xi f_0}{p}+\frac{1-\xi^2}{p}\frac{\partial f_0}{\partial\xi}-\frac{2\xi f_0}{p}\right]\\ &= 2\frac{e\langle\boldsymbol{E}\cdot\boldsymbol{B}\rangle}{\nu_{\mathrm{D}}B}\frac{\partial f_0}{\partial p}\xi,\end{aligned} \tag{3.16}$$

which we can integrate over ξ, from -1 to ξ, to obtain

$$\left(1-\xi^2\right)\frac{\partial f_1}{\partial\xi} = -\frac{e\langle\boldsymbol{E}\cdot\boldsymbol{B}\rangle}{\nu_{\mathrm{D}}B}\frac{\partial f_0}{\partial p}\left(1-\xi^2\right) \tag{3.17a}$$

$$\implies \frac{\partial f_1}{\partial\xi} = -\frac{e\langle\boldsymbol{E}\cdot\boldsymbol{B}\rangle}{\nu_{\mathrm{D}}B}\frac{\partial f_0}{\partial p}. \tag{3.17b}$$

Once again, we integrate from -1 to ξ to obtain

$$f_1 = -\frac{e\langle\boldsymbol{E}\cdot\boldsymbol{B}\rangle}{\nu_{\mathrm{D}}B}\frac{\partial f_0}{\partial p}\left(\xi+1\right), \tag{3.18}$$

and this expression we can insert into equation (3.15c). Before doing this, however, we integrate (3.15c) over pitch angle

$$\frac{1}{2}\int_{-1}^{1}\frac{\partial f_0}{\partial t}\mathrm{d}\xi = -\frac{1}{2}\int_{-1}^{1}\frac{e\langle\boldsymbol{E}\cdot\boldsymbol{B}\rangle}{B}\frac{\xi}{p^2}\frac{\partial\left(p^2 f_1\right)}{\partial p}\mathrm{d}\xi \tag{3.19a}$$

$$+\frac{1}{2}\int_{-1}^{1}\frac{\partial}{\partial\xi}\left[\left(1-\xi^2\right)\left(\frac{\nu_{\mathrm{D}}}{2}\frac{\partial f_2}{\partial\xi}-\frac{e\langle\boldsymbol{E}\cdot\boldsymbol{B}\rangle}{B}\frac{f_1}{p}\right)-\langle A_{\mathrm{S}}^{\xi}\rangle f_0\right]\mathrm{d}\xi \tag{3.19b}$$

$$+\frac{1}{2}\int_{-1}^{1}\left\{\frac{1}{p^2}\frac{\partial}{\partial p}\left[p^2\left(-\langle\hat{A}^p\rangle f_0+\langle D^{pp}\rangle\frac{\partial f_0}{\partial p}\right)\right]+\frac{1}{V'}\frac{\partial}{\partial r}\left[V'\left(-\langle A^r\rangle f_0+\langle D^{rr}\rangle\frac{\partial f_0}{\partial r}\right)\right]+\langle S\rangle\right\}\mathrm{d}\xi. \tag{3.19c}$$

Since f_0 does not depend on pitch angle, the left hand side of equation (3.19) is equal to its integrand. For (3.19c), we only need to average the advection and diffusion coefficients, as well as the source term, with regard to pitch angle, and these averages we denote by $\langle\cdot\rangle_\xi$. The term (3.19b) is zero, since the factor $\left(1-\xi^2\right)$ is zero at the integral boundaries, and also $\langle A_{\mathrm{S}}^{\xi}\rangle \propto \left(1-\xi^2\right)$. Finally, if we insert the expression for f_1, i.e. (3.18), into the first term on the right hand side, we obtain

$$\begin{aligned}(3.19\mathrm{a}) &= \frac{1}{p^2}\frac{\partial}{\partial p}\left(p^2\frac{e^2\langle\boldsymbol{E}\cdot\boldsymbol{B}\rangle^2}{\nu_{\mathrm{D}}B^2}\frac{\partial f_0}{\partial p}\right)\int_{-1}^{1}\frac{\xi\left(\xi+1\right)}{2}\mathrm{d}\xi\\ &= \frac{1}{p^2}\frac{\partial}{\partial p}\left(p^2\frac{e^2\langle\boldsymbol{E}\cdot\boldsymbol{B}\rangle^2}{3\nu_{\mathrm{D}}B^2}\frac{\partial f_0}{\partial p}\right).\end{aligned} \tag{3.20}$$

The final reduced kinetic equation is thus

$$\begin{aligned}\frac{\partial f_{\mathrm{st}}}{\partial t} = \frac{1}{p^2}\frac{\partial}{\partial p}\left[p^2\left(-\langle \hat{A}^p\rangle_\xi f_{\mathrm{st}} + \left(\langle D^{pp}\rangle_\xi + \frac{e^2\langle \boldsymbol{E}\cdot\boldsymbol{B}\rangle^2}{3\nu_{\mathrm{D}}B^2}\right)\frac{\partial f_{\mathrm{st}}}{\partial p}\right)\right] \\ + \frac{1}{V'}\frac{\partial}{\partial r}\left[V'\left(-\langle A^r\rangle_\xi f_{\mathrm{st}} + \langle D^{rr}\rangle_\xi \frac{\partial f_{\mathrm{st}}}{\partial r}\right)\right] + \langle S\rangle_\xi.\end{aligned} \tag{3.21}$$

Notably, in this equation the electric field takes the form of a diffusion operator, rather than the conventional advection operator in equation (3.11).

Since the leading order term of the distribution function is isotropic, it can not carry a current. Instead, the current has to be evaluated using the next order term (f_1), given in equation (3.18), according to

$$\begin{aligned} j_1 &= 2\pi\frac{e^2\langle \boldsymbol{E}\cdot\boldsymbol{B}\rangle}{B}\int_0^\infty\int_{-1}^1 \xi(1+\xi)\frac{v(p)p^2}{\nu_{\mathrm{D}}}\frac{\partial f_{\mathrm{st}}}{\partial p}\mathrm{d}\xi\mathrm{d}p \\ &= \frac{2\pi}{3}\frac{e^2\langle \boldsymbol{E}\cdot\boldsymbol{B}\rangle}{B}\int_0^\infty \frac{v(p)p^2}{\nu_{\mathrm{D}}}\frac{\partial f_{\mathrm{st}}}{\partial p}\mathrm{d}p.\end{aligned} \tag{3.22}$$

If f_1 is large at momenta where the assumption of $\langle \boldsymbol{E}\cdot\boldsymbol{B}\rangle/(B\nu_{\mathrm{d}}(p)) \sim \delta^1$ is no longer valid, the current density obtained from this expression can be unreasonably high, since f_1 does not conserve particle density. When the current density is overestimated by equation (3.22), we could get a better approximation of the current density value from f_{st} (still evaluated using (3.21)) by assuming that all superthermal electrons travel parallel to the magnetic field lines, i.e.

$$j_2 = 4\pi e\ \mathrm{sgn}\left(\langle \boldsymbol{E}\cdot\boldsymbol{B}\rangle\right)\int_0^\infty v(p)p^2 f_{\mathrm{st}}\mathrm{d}p. \tag{3.23}$$

Thus, to get a good and reasonably bounded estimation of the superthermal current density, we use

$$j_{\mathrm{st}} = \frac{j_1 j_2}{\sqrt{j_1^2 + j_2^2}}. \tag{3.24}$$

Since the driving forces behind the runaway phenomenon, namely the interplay between electric field acceleration and collisional friction, are included in the kinetic equation (3.21), the runaway seed generation is implicitly modelled as part of the momentum space particle flux. The flux of particles from the superthermal to the runaway electron population is found to be

$$\phi^p_{\mathrm{st}} = 4\pi V' p_{\mathrm{re}}^2\left[-\langle \hat{A}^p\rangle_\xi f_{\mathrm{st}} + \left(\langle D^{pp}\rangle_\xi + \frac{e^2\langle \boldsymbol{E}\cdot\boldsymbol{B}\rangle^2}{3\nu_{\mathrm{D}}B^2}\right)\frac{\partial f_{\mathrm{st}}}{\partial p}\right]_{p=p_{\mathrm{re}}}, \tag{3.25}$$

i.e. it is the momentum space particle flux through the upper boundary p_{re} of the momentum grid on which the superthermal population is defined. This momentum space particle flux includes both hot-tail and Dreicer generation, as well as seed generation from tritium beta decay and Compton scattering during activated operation.

To include the activated seed generation mechanisms, it is necessary to model the generation of superthermal electrons from these activated processes

through source terms in the kinetic equation (3.21). These source terms are derived in paper C, and a more detailed description of the physics behind these generation mechanisms can be found in sections 2.3 and 2.4. The source term due to tritium beta decay depends on the tritium particle density n_{T} and tritium half life τ_{T} according to

$$\langle S_{\mathrm{T}} \rangle = C \frac{\ln 2}{4\pi} \frac{n_{\mathrm{T}}}{\tau_{\mathrm{T}}} \frac{1}{p^2} \frac{p\gamma \left(\gamma_{\max} - \gamma\right)^2}{1 - \exp(-4\pi\alpha/\beta)} \Theta(p_{\max} - p), \tag{3.26}$$

where α is the fine structure constant, $\beta = p/\gamma$ is the normalized speed and C is a proportionality constant used to ensure that the total generation rate is $\ln 2 \cdot n_{\mathrm{T}}/\tau_{\mathrm{T}}$. The maximum momentum $p_{\max}$ and Lorentz factor $\gamma_{\max}$ correspond to the maximum energy, $W_{\max}$ of an emitted beta electron. For the Compton scattering, we instead consider the photon energy spectrum Γ_γ, which depends on machine design and plasma composition, and the total number of electrons available for photons to scatter on $n_{\mathrm{e,tot}}$. The source term can be shown to take the form

$$\langle S_{\mathrm{C}} \rangle = \frac{n_{\mathrm{e,tot}}}{2} \frac{1}{p^2} \int_{W_{\gamma 0}}^{\infty} \Gamma_\gamma(W_\gamma) \frac{\mathrm{d}\sigma}{\mathrm{d}\Omega} \frac{\beta}{\left(\frac{W_\gamma}{m_{\mathrm{e}}c^2} + 1 - \gamma\right)^2} \mathrm{d}W_\gamma, \tag{3.27}$$

where $\mathrm{d}\sigma/\mathrm{d}\Omega$ is the Klein-Nishina differential cross section [37] and W_γ is the photon energy.

Runaway electrons

When seed generation is modelled kinetically by evolving the superthermal electron population, the runaway electron density

$$\frac{\partial n_{\mathrm{re}}}{\partial t} = \Gamma_{\mathrm{ava}} n_{\mathrm{re}} + \phi_{\mathrm{st}}^p + \gamma_{\mathrm{C}} + \frac{1}{V'} \frac{\partial}{\partial r} \left[V' \langle D^{rr} \rangle \frac{\partial n_{\mathrm{re}}}{\partial r} \right], \tag{3.28}$$

where ϕ_{st}^p describes the runaway seed generation as in (3.25), and

$$\gamma_{\mathrm{C}} = \int_{p > p_{\mathrm{re}}} \langle S_{\mathrm{C}} \rangle \, \mathrm{d}^3\boldsymbol{p}. \tag{3.29}$$

There is no corresponding term for tritium beta decay, since p_{re} should be chosen such that $p_{\max} < p_{\mathrm{re}}$, meaning that all electrons generated by tritium beta decay are generated within the superthermal momentum range.

When the runaway seed generation is not modelled kinetically, all seed generation mechanisms need to be modelled as generation rates, and the runaway electron seed generation is instead replaced by

$$\phi_{\mathrm{st}}^p + \gamma_{\mathrm{C}} \rightarrow \gamma_{\mathrm{D}} + \gamma_{\mathrm{ht}} + \gamma_{\mathrm{T}} + \gamma_{\mathrm{C}}. \tag{3.30}$$

The Dreicer generation is described by γ_{D}, which for electric fields $E \gg E_{\mathrm{c}}$ can be estimated [23] by equation (2.3) in section 2.1. However, this expression overestimates the generation rate for lower electric field strengths. To achieve

Dreicer generation rates with comparable accuracy to that of kinetic modelling, even for lower electric field strengths, we instead use a neural network trained on kinetic simulations [26]. For an analytical expression to estimate the hot-tail generation rate γ_{ht}, we use (2.25), derived in section 2.2, i.e.

$$\gamma_{\mathrm{ht}} = -4\pi p_{\mathrm{c}}^2 \frac{\partial p_{\mathrm{c}}}{\partial t} \frac{n_{\mathrm{free},0}}{\pi^{3/2} p_{\mathrm{th},0}^3} \exp\left[-\frac{\left(p^3 + 3\tau(t)\right)^{2/3}}{p_{\mathrm{th},0}^2} \right], \tag{3.31}$$

where p_{c} is the critical momentum for runaway electron generation, $p_{\mathrm{th},0}$ is the initial thermal momentum, n_{free} is the initial free electron density and $\tau(t)$ is the time integrated collision frequency. Finally, the tritium beta decay and Compton scattering generation rates are determined according to the same principles as the kinetic sources in equations (3.26) and (3.27), only they are integrated in momentum space from the critical momentum [35, 36], i.e.

$$\gamma_{\mathrm{T/C}} = \int_{p>p_{\mathrm{c}}} \langle S_{\mathrm{T/C}} \rangle \, \mathrm{d}^3\boldsymbol{p}. \tag{3.32}$$

Since it is mainly electrons with $p > p_{\mathrm{re}}$ that contribute to the avalanche multiplication, avalanche generation cannot be accurately described kinetically using the distribution of the superthermal electrons. Instead, it is modelled as a growth rate term, i.e. the $\Gamma_{\mathrm{ava}} n_{\mathrm{re}}$ in equations (3.28). The avalanche growth rate is determined from the electron density and electric field, according to

$$\Gamma_{\mathrm{ava}} = \frac{e}{m_{\mathrm{e}} c \ln\Lambda_{\mathrm{c}}} \frac{n_{\mathrm{e,tot}}}{n_{\mathrm{th}}} \frac{E_{\parallel} - E_{\mathrm{c}}^{\mathrm{eff}}}{\sqrt{4 + \bar{\nu}_s(p_{\mathrm{c}}^\star)\bar{\nu}_D(p_{\mathrm{c}}^\star)}}, \tag{3.33}$$

as described in section 2.5 [38].

Temperature

In this disruption model, the plasma temperature is defined through the energy density W_{th} of the thermal (bulk) electron population as $T_{\mathrm{th}} = 2W_{\mathrm{th}}/3n_{\mathrm{th}}$. Its evolution is governed by the energy balance equation

$$\begin{aligned} \frac{\partial W_{\mathrm{th}}}{\partial t} = \frac{j\Omega}{B} \langle \boldsymbol{E} \cdot \boldsymbol{B} \rangle - n_{\mathrm{th}} \sum_i \sum_{j=0}^{Z_i - 1} n_i^{(j)} L_i^{(j)} + \langle Q_{\mathrm{c}} \rangle \\ + \frac{1}{V'} \frac{\partial}{\partial r} \left[V' \langle D^{rr} \rangle \frac{3n_{\mathrm{th}}}{2} \frac{\partial T_{\mathrm{th}}}{\partial r} \right]. \end{aligned} \tag{3.34}$$

There are two heating terms in this temperature evolution model. The first term of equation (3.34) represents the Ohmic heating, i.e. the heating of the plasma due to the electron-ion collision induced resistance to the thermal part of the plasma current. Notably, the Ohmic heating is stronger at low plasma temperatures, due to the resistivity of the plasma $\propto T^{-3/2}$. Additionally, the thermal electron population can be heated through collisions with ions,

superthermal and runaway electrons. Heating from collisions with superthermal electrons is described by

$$\langle Q_{\mathrm{c,st}} \rangle = 16\pi^2 n_{\mathrm{th}} r_{\mathrm{e}}^2 m_{\mathrm{e}} c^4 \int \ln \Lambda_{\mathrm{ee}} \frac{p^2}{v} f_{\mathrm{st}} \mathrm{d}p, \tag{3.35}$$

with r_{e} being the classical electron radius and $\ln \Lambda_{\mathrm{ee}}$ the electron-electron Coulomb logarithm [40]. Assuming that all runaway electrons travel at the speed of light, the heating from collisions with runaway electrons can be estimated by

$$\langle Q_{\mathrm{c,re}} \rangle = ecE_{\mathrm{c}} n_{\mathrm{re}}, \tag{3.36}$$

where E_{c} is the Connor-Hastie field. For collisions with ions, the heating term is a sum over all ion species, i.e.

$$\langle Q_{\mathrm{c,ions}} \rangle = \sum_i \langle Q_{ei} \rangle, \tag{3.37}$$

where the heat transfer $\langle Q_{ei} \rangle$ to particle species k from collisions with particle species l is

$$Q_{kl} = \left(\sum_{j=0}^{Z_k} n_k^{(j)} Z_{0j}^2 \right) \left(\sum_{j=0}^{Z_l} n_l^{(j)} Z_{0j}^2 \right) \frac{e^4 \ln \Lambda_{kl}}{(2\pi)^{3/2} \epsilon_0^2 m_k m_l} \frac{T_l - T_k}{\left(\frac{T_k}{m_k} + \frac{T_l}{m_l} \right)^{3/2}}, \tag{3.38}$$

with the Coulomb logarithm $\ln \Lambda_{kl}$ representing collisions between particles of species k and l [40]. Here, Z_i denotes atomic number and Z_{0j} denotes charge number for charge state j, $n_i^{(j)}$ denotes the ion density of charge state j, m_i denotes particle mass and T_i species temperature.

The thermal population is cooled through inelastic atomic processes – namely radiation, ionization and recombination – and heat transport. Heat transport is modelled through the last term on the left hand side of equation (3.34), and is described in detail in the section on transport. The inelastic processes are modelled through the second term of (3.34), where for ions of species i and charge state j

$$L_i^{(j)} = L_{\mathrm{rad}} + \Delta W_i^{(j)} \left(I_i^{(j)} - R_i^{(j)} \right). \tag{3.39}$$

Here, L_{rad} is the heat loss due to line and recombination radiation, as well as radiation due to bremsstrahlung. The ionization threshold $\Delta W_i^{(j)}$, obtained from the NIST database [42], together with the ionization rate $I_i^{(j)}$ and recombination rate $R_i^{(j)}$, yields the heat loss due to changes in potential energy. The ionization and recombination rates are obtained from the AMJUEL database [43] for hydrogen isotopes, which accounts for opacity effects, and from the OpenADAS database for other ion species [44].

Similarly, the ion temperatures are evolved according to equipartition, $W_i = 3n_i T_i/2$, where for ion species i

$$\frac{\partial W_i}{\partial t} = \langle Q_{\mathrm{ie}} \rangle + \sum_k \langle Q_{ik} \rangle. \tag{3.40}$$

The ion densities are evolved through modelling ionization and recombination, using the $I_i^{(j)}$ and $R_i^{(j)}$ rates above, according to

$$\frac{\partial n_i^{(j)}}{\partial t} = \left(I_i^{(j-1)} n_{\mathrm{th}} + \langle \mathcal{I}_i^{(j-1)} f_{\mathrm{st}} \rangle\right) n_i^{(j-1)} - \left(I_i^{(j)} n_{\mathrm{th}} + \langle \mathcal{I}_i^{(j)} f_{\mathrm{st}} \rangle\right) n_i^{(j)} + R_i^{(j+1)} n_{\mathrm{th}} n_i^{j+1} - R_i^{(j)} n_{\mathrm{th}} n_i^{(j)}. \tag{3.41}$$

Notably, we also consider kinetic ionization due to collisions between ions and superthermal electrons, which is described by

$$\langle \mathcal{I}_i^{(j)} f_{\mathrm{st}} \rangle = 4\pi \int p^2 \sigma_{\mathrm{ion},i}^{(j)} v f_{\mathrm{st}} \, \mathrm{d}p, \tag{3.42}$$

where $\sigma_{\mathrm{ion},i}^{(j)}$is the ionization cross section [45].

Transport

During the thermal quench, when the magnetic surfaces are broken up and field lines are stochastic, there is significant radial transport of runaway electrons, superthermal electrons and thermal energy. For self-consistent modelling of the transport dynamics, higher dimensionality than used in this plasma model is required, both spatially and with regard to velocity. Instead, we rely on analytical formulas to estimate the particle and heat transport losses. We have used the Rechester–Rosenbluth diffusion model, with diffusion coefficient [46]

$$D^{rr} = \pi q R_0 |v_\parallel| \left(\frac{\delta B}{B}\right)^2, \tag{3.43}$$

and no advection, i.e. $A^r = 0$. Here, q is the safety factor. The magnetic stochastization is quantified through the relative amplitude of the magnetic perturbation, $\delta B/B$, which is assumed to be spatially and temporally constant during the thermal quench for simplicity. As we evolve the velocity distribution of the superthermal electrons, in equation (3.21), the diffusion coefficient is exactly as described by equation (3.43). For the thermal energy transport, in equation (3.34), the parallel velocity can be shown to be approximately the thermal speed, derived using the fact that the thermal bulk is Maxwellian [40]. The runaway electrons are assumed to travel parallel to the magnetic field lines at the speed of light, meaning that for the diffusion coefficient D^{rr} of equations (3.28), $v_\parallel = c$. As this transport neither accounts for the pitch angle dependence of the runaway electron transport, nor for finite Larmor radius and orbit width effects [47], this gives an upper boundary of the runaway electron transport [48].

3.2 Modelling start-up

The physics can mostly be modelled similarly for tokamak disruptions and start-up, except for three key differences that need to be taken into consideration.

Firstly, a strong, externally induced electric field is applied during the start-up, to ionize the fuel gas and initiate the plasma. Secondly, during the ionization phase, neutral particles are screened out of the core of the plasma, which affects the density and energy balance. Finally, there will be anomalously high particle transport before the flux surfaces have been properly formed, which needs to be accounted for. Here, we present the start-up model used in paper A, which derives from the plasma model used for disruptions.

The start-up model is 0D, meaning that both the spatial and momentum dependence of the plasma evolution are neglected. The main reason for not retaining the radial dependence of the plasma evolution, as is done in the disruption model, is the model that is used to accounting for neutral screening. Neutral particles can exist both in the outer part of the plasma, as well as in the vessel volume, while the charged particles are confined to the plasma. Spatially, the plasma models used in this thesis only consider the plasma, and not the whole vessel volume. Accounting for the effect of neutral screening would complicate the density and energy balance equations if the spatial dependence would be considered, due to the complicated geometry of the non plasma part of the vacuum vessel.

Electric field and currents

When modelling the electric field during start-up, the electric field evolution should account for the external electric field applied to initiate the plasma. If the spatial dependence of the plasma evolution is neglected, meaning that we assume a 0D plasma model, circuit theory can be used to determine the electric field evolution, under the influence of the externally applied loop voltage U_{ext}.

The circuit equations can be derived from the electric field and current model used for disruptions ((3.5) – (3.9)), i.e.

$$U = 2\pi \frac{\langle \boldsymbol{E} \cdot \boldsymbol{B} \rangle}{\langle \boldsymbol{B} \cdot \nabla \varphi \rangle}, \tag{3.44a}$$

$$\frac{\partial \psi}{\partial t} = U, \tag{3.44b}$$

$$2\pi\mu_0 \langle \boldsymbol{B} \cdot \nabla \varphi \rangle \frac{j_{\text{tot}}}{B} = \frac{1}{V'} \frac{\partial}{\partial r} \left[V' \left\langle \frac{|\nabla r|^2}{R^2} \right\rangle \frac{\partial \psi}{\partial r} \right], \tag{3.44c}$$

$$I_{\text{p}} = \frac{1}{2\pi} \int_0^a V' \langle \boldsymbol{B} \cdot \nabla \varphi \rangle \frac{j_{\text{tot}}}{B} \mathrm{d}r, \tag{3.44d}$$

$$\psi_{\text{wall}} = \psi_{\text{sym}} - L_{\text{ext}}(I_{\text{p}} + I_{\text{wall}}), \tag{3.44e}$$

$$U_{\text{wall}} = R_{\text{wall}} I_{\text{wall}}. \tag{3.44f}$$

Notably, equation (3.44e) contains a term ψ_{sym} compared to (3.7b), which describes the poloidal flux at the symmetry axis $R = 0$. In the disruption model, we defined $\psi(r) = 2\pi \int_0^{R(r)} (\boldsymbol{B} \cdot \hat{Z})\, R \,\mathrm{d}R$ such that $\psi_{\text{sym}} = \psi(R = 0) = 0$. However, if we want to consider an externally applied loop voltage we can instead introduce a uniform offset, such that $\psi(r) = \psi_{\text{ext}} + 2\pi \int_0^{R(r)} (\boldsymbol{B} \cdot \hat{Z})\, R \,\mathrm{d}R$,

where

$$\frac{\partial \psi_{\text{ext}}}{\partial t} = U_{\text{ext}} \tag{3.45}$$

in accordance with Faraday's law. Here, we assume the central solenoid responsible for inducing the applied electric field is a line source aligned with the symmetry axis, as opposed to having a finite width. Note that including ψ_{ext} in the poloidal flux does not change the magnetic field. Importantly, the poloidal magnetic flux at the symmetry axis $\psi_{\text{sym}} = \psi_{\text{ext}}$, and is in general time dependent.

Starting from the total parallel current density j_{tot}, we can integrate equation (3.44c) over the plasma cross section in accordance with equation (3.44d), i.e.

$$2\pi\mu_0 \int_0^r V' \langle \boldsymbol{B} \cdot \nabla\varphi \rangle \frac{j_{\text{tot}}}{B} \mathrm{d}r' = \int_0^r V' \frac{1}{V'} \frac{\partial}{\partial r'} \left[V' \left\langle \frac{|\nabla r'|^2}{R^2} \right\rangle \frac{\partial \psi}{\partial r'} \right] \mathrm{d}r' \tag{3.46a}$$

$$\implies (2\pi)^2 \mu_0 I(r) = V' \left\langle \frac{|\nabla r|^2}{R^2} \right\rangle \frac{\partial \psi}{\partial r} \tag{3.46b}$$

$$\implies \frac{\partial \psi}{\partial r} = \frac{1}{V' \left\langle |\nabla r|^2 / R^2 \right\rangle} (2\pi)^2 \mu_0 I(r), \tag{3.46c}$$

where $I(r)$ is the plasma current enclosed within the flux surface with minor radius r. Note that in equation (3.46a), the integrand will be zero at $r = 0$ since $V'(r = 0) = 0$.

The solution to the differential equation (3.46c)

$$\psi(r) \equiv \psi = \psi(r_0) + (2\pi)^2 \mu_0 \int_{r_0}^r \frac{I(r')\mathrm{d}r'}{V' \left\langle |\nabla r'|^2 / R^2 \right\rangle}, \tag{3.47}$$

where r_0 is an arbitrary minor radius. If we now only consider the poloidal flux outside of the plasma ($r > a$), choosing $r_0 = a$ and noting that $I(r > a) = I(a) = I_{\text{p}}$, we obtain

$$\psi = \psi(a) + (2\pi)^2 \mu_0 I_{\text{p}} \int_a^r \frac{\mathrm{d}r'}{V' \left\langle |\nabla r'|^2 / R^2 \right\rangle} = \psi(a) + L_{\text{e}}(r) I_{\text{p}}. \tag{3.48}$$

Here we have introduced the inductance variable L_{e}, representing the inductance between the plasma edge and the open flux surface with minor radius r. At the tokamak wall ($r = b$),

$$\psi_{\text{wall}} = \psi(a) + L_{\text{ew}} I_{\text{p}}, \tag{3.49}$$

with the inductance parameter L_{ew}, representing the inductance between the plasma edge and the wall.

Using Faraday's law (3.44b) on equations (3.48) and (3.49), as well as (3.44e), we obtain three expressions for the loop voltages

$$U = U(a) + L_\mathrm{e}\frac{\mathrm{d}I_\mathrm{p}}{\mathrm{d}t}, \tag{3.50a}$$

$$U_\mathrm{wall} = U(a) + L_\mathrm{ew}\frac{\mathrm{d}I_\mathrm{p}}{\mathrm{d}t}, \tag{3.50b}$$

$$U_\mathrm{wall} = U_\mathrm{ext} - L_\mathrm{ext}\left(\frac{\mathrm{d}I_\mathrm{p}}{\mathrm{d}t} + \frac{\mathrm{d}I_\mathrm{wall}}{\mathrm{d}t}\right), \tag{3.50c}$$

which can be combined into a single circuit equation relating all voltages and currents, namely

$$U_\mathrm{ext} = U + (L_\mathrm{ext} + L_\mathrm{ew} - L_\mathrm{e})\frac{\mathrm{d}I_\mathrm{p}}{\mathrm{d}t} + L_\mathrm{ext}\frac{\mathrm{d}I_\mathrm{wall}}{\mathrm{d}t}. \tag{3.51}$$

Furthermore, in 0D, equation (3.44a) is simplified to

$$U = 2\pi\frac{\langle \boldsymbol{E}\cdot\boldsymbol{B}\rangle}{\langle \boldsymbol{B}\cdot\nabla\varphi\rangle} \to 2\pi\frac{E_\parallel\cdot B}{B\cdot 1/R_0} = 2\pi R_0 E_\parallel. \tag{3.52}$$

If we instead combine (3.50c) with equation (3.44f), we get

$$U_\mathrm{ext} = R_\mathrm{wall}I_\mathrm{wall} + L_\mathrm{ext}\left(\frac{\mathrm{d}I_\mathrm{p}}{\mathrm{d}t} + \frac{\mathrm{d}I_\mathrm{wall}}{\mathrm{d}t}\right). \tag{3.53}$$

Equations (3.51) and (3.53) give the general form of the circuit equations used for the start-up electric field model. However, this approach assumes that the tokamak wall is shaped in the same way as the plasma, which is typically not the case. To account for arbitrary vessel shapes, the inductances can be replaced with more general expressions, as is done in for example the DYON start-up simulation code [11]. More specifically, the circuit equations used for evolving the electric field, as well as the plasma and wall currents in the tokamak start-up model are

$$U_\mathrm{ext} = 2\pi R_0 E_\parallel + L_\mathrm{p}\frac{\mathrm{d}I_\mathrm{p}}{\mathrm{d}t} + M\frac{\mathrm{d}I_\mathrm{wall}}{\mathrm{d}t}, \tag{3.54a}$$

$$U_\mathrm{ext} = R_\mathrm{wall}I_\mathrm{wall} + M\frac{\mathrm{d}I_\mathrm{p}}{\mathrm{d}t} + L_\mathrm{wall}\frac{\mathrm{d}I_\mathrm{wall}}{\mathrm{d}t}, \tag{3.54b}$$

where the plasma inductance L_p, wall inductance L_wall, plasma-wall mutual inductance M and wall resistivity R_wall are free parameters.

Transport

Closed flux surfaces are formed during the burn-through phase of the plasma discharge, which greatly improves particle confinement. At the beginning of the burn-through phase, the magnetic field lines are open, and the main particle losses occur along these field lines. When closed flux surfaces have formed, however, transport perpendicular to the field lines dominates. Transport is

accounted for in the density and temperature evolution of the ions and electrons. Details of the modified expressions for the temperature and density evolution can be found in the following sections. The transport rate of a quantity X can be estimated by X/τ, where τ is the confinement time.

To account for both parallel and perpendicular losses of ions, we define the ion confinement time τ_i such that

$$\frac{1}{\tau_\mathrm{i}} = \frac{1}{\tau_\mathrm{i}^{\parallel}} + \frac{1}{\tau_\mathrm{i}^{\perp}}. \tag{3.55}$$

When parallel losses dominate, the parallel confinement time $\tau_\mathrm{i}^{\parallel}$ is short and $\tau_\mathrm{i} \approx \tau_\mathrm{i}^{\parallel}$, while analogously, when perpendicular losses dominate $\tau_\mathrm{i} \approx \tau_\mathrm{i}^{\perp}$. The parallel transport during the burn-through phase can be described by transsonic ambipolar flow along the field lines [11]. This enables us to evaluate the confinement time from the effective distance the ions travel before leaving the plasma, i.e. the connection length L_eff, and the effective speed at which the ions travel, namely the sound speed of the main ion species C_s, as

$$\tau_\mathrm{i}^{\parallel} = \frac{L_\mathrm{eff}}{C_\mathrm{s}}. \tag{3.56}$$

The sound speed of the main ion species is evaluated as

$$C_\mathrm{s} = \sqrt{\frac{T_\mathrm{th} + T_\mathrm{m}}{m_\mathrm{m}}}, \tag{3.57}$$

where T_m and m_m are the temperature and mass of the main ion species, respectively. The effective connection length is determined by the plasma minor radius and the magnetic field configuration, which in turn is affected by the plasma current evolution. As the plasma current increases, the effect of stray magnetic fields caused by currents in plasma-facing conducting structures (so called eddy currents) on the magnetic configuration decreases and closed flux surfaces start to form. More specifically, the effective connection length can be estimated by [11, 49, 50]

$$L_\mathrm{eff} = \frac{3a(t)}{4} \frac{B_\varphi}{B_z(t)} \exp\left(\frac{I_\mathrm{p}(t)}{I_\mathrm{ref}}\right), \tag{3.58}$$

where B_φ is the toroidal magnetic field strength. The parameter I_ref represents the plasma current value at which point the flux surfaces have formed, which happens when the plasma current exceeds the eddy currents in the wall. Thus, I_ref can be estimated from the maximum eddy currents feasible in the surrounding structure of the specific machine [11]. Notably, the connection length evolves in time through the plasma current I_p, the stray magnetic field $B_z(t)$ – consisting of the vertical magnetic field B_v and eddy current induced magnetic field $B_\mathrm{eddy}(t)$ – and through the minor radius $a(t)$ of the outermost closed flux surface.

The perpendicular particle transport is described by Bohm diffusion [51], which is collisional diffusion in the high-collisionality regime. The perpendicular

confinement time is evaluated from the Bohm velocity v_{Bohm}, which stems from the Bohm diffusion coefficient D_{Bohm} as $v_{\mathrm{Bohm}} = 2D_{\mathrm{Bohm}}/a$, and the plasma minor radius as

$$\tau_{\mathrm{i}}^{\perp} = \frac{a(t)}{v_{\mathrm{Bohm}}(t)} = \frac{a(t)^2}{2D_{\mathrm{Bohm}}(t)}, \tag{3.59}$$

where

$$D_{\mathrm{Bohm}} = \frac{1}{16}\frac{T_{\mathrm{th}}(t)}{eB_{\varphi}}. \tag{3.60}$$

The confinement time for thermal electrons τ_{e} is assumed to be equal to the ion confinement time, due to ambipolarity, but it is different for the runaway electrons, as they are travelling at much higher speeds. Similarly to ions and thermal electrons, the runaway electron losses are dominated by parallel transport when the magnetic field lines are open, with the same effective connection length L_{eff}. However, the runaway electrons can not be assumed to travel at a constant velocity, as they are freely accelerated by the electric field $E_{\parallel}$ according to

$$\frac{\mathrm{d}p}{\mathrm{d}t} = eE_{\parallel}. \tag{3.61}$$

Assuming that the electric field varies slowly on the timescales of runaway electron acceleration, we can integrate equation (3.61) in time and solve for the velocity, we obtain the time evolution of the velocity of a runaway electron

$$v = \frac{eE_{\parallel}t/m_{\mathrm{e}}}{\sqrt{1+\left(\frac{eE_{\parallel}t}{m_{\mathrm{e}}c}\right)^2}}. \tag{3.62}$$

Integrating this velocity over the runaway electron confinement time $\tau_{\mathrm{re}}^{\parallel}$ yields the effective connection length

$$L_{\mathrm{eff}} = \frac{m_{\mathrm{e}}c^2}{eE_{\parallel}}\left[\sqrt{1+\left(\frac{eE_{\parallel}\tau_{\mathrm{re}}^{\parallel}}{m_{\mathrm{e}}c}\right)^2}-1\right], \tag{3.63}$$

from which we can solve for the confinement time to obtain

$$\tau_{\mathrm{re}}^{\parallel} = \frac{m_{\mathrm{e}}c}{eE_{\parallel}}\sqrt{\left(\frac{eE_{\parallel}L_{\mathrm{eff}}}{m_{\mathrm{e}}c^2}+1\right)^2-1}. \tag{3.64}$$

When the flux surfaces have formed, the transport of runaway electrons is instead dominated by drift effects caused by the increasing kinetic energy of the runaway – as the energy is increased, the particle orbits are shifted out of the plasma. Based on the conservation of the toroidal momentum (equation (4.16) of Ref. [16]) it can be argued that the maximum energy possible for a runaway electron to have before its orbit intersects the plasma wall is

$$\gamma_{\mathrm{max}} \approx 5.6\times10^{-5}\frac{R_0}{a(t)}I_{\mathrm{p}}(t)\,[\mathrm{A}]. \tag{3.65}$$

If we integrate equation (3.61) over the drift confinement time $\tau_{\mathrm{re}}^{\mathrm{d}}$, we get the corresponding maximum momentum

$$p_{\max} = \int_0^{\tau_{\mathrm{re}}^{\mathrm{d}}} eE_{\parallel} \mathrm{d}t = eE_{\parallel}\tau_{\mathrm{re}}^{\mathrm{d}}. \tag{3.66}$$

For runaway energies, we can use the approximation $p_{\max} \approx m_{\mathrm{e}} c \gamma_{\max}$, which yields the drift confinement time

$$\tau_{\mathrm{re}}^{\mathrm{d}} \approx 10^{-7} \frac{R_0}{a} \frac{I_{\mathrm{p}}(t)\,[\mathrm{A}]}{E_{\parallel}\,[\mathrm{V/m}]}. \tag{3.67}$$

In order for the parallel transport to dominate before the flux surfaces have formed, and drift transport after, we interpolate between the two using the same plasma current criteria as for the connection length, i.e.

$$\frac{1}{\tau_{\mathrm{re}}} = \frac{\exp\left(I_{\mathrm{p}}(t)/I_{\mathrm{ref}}\right)}{\tau_{\mathrm{re}}^{\parallel}} + \frac{1 - \exp\left(I_{\mathrm{p}}(t)/I_{\mathrm{ref}}\right)}{\tau_{\mathrm{re}}^{\mathrm{d}}}. \tag{3.68}$$

Two volume method

After the breakdown phase, but prior to burn-through, the mean free path for ionization of neutrals decreases. This means that the volume surrounding the centre of the plasma solely consists of ions, while neutrals are only present outside of the plasma core. This neutral screening effect needs to be taken into consideration when modelling the density flux between neutrals and ions through ionization, recombination and charge exchange, since the volume occupied by neutrals is different to the volume occupied by ions. In the start-up model used in paper A, we utilize the two volume method [52], which estimates the part of the plasma volume $V_{\mathrm{n},i}$ where neutrals of ion species i remain, based on the mean free path of the neutral being ionized by an electron. To get an accurate evolution of the density and kinetic energy, ionization, recombination and charge exchange rates are weighted with the proportionality between the volume where the reaction can occur and the volume where the resulting ion or neutral can exist. More specifically, the weighting factors are needed to ensure that the densities (and energy densities) integrate to the correct total particle numbers (and energy), as different particle species occupy different subsets of the tokamak vessel volume.

The relevant volumes of this method are illustrated in figure 3.1. The vacuum vessel of the plasma has the volume V_{vv}. The plasma volume V_{p} is a subset of the vacuum vessel volume, and notably, it contains both charged and neutral particles, and is evaluated as

$$V_{\mathrm{p}}(t) = \int_0^{a(t)} \mathrm{d}r \int_0^{2\pi} \mathrm{d}\varphi \int_{-\pi}^{\pi} \mathcal{J} \mathrm{d}\theta, \tag{3.69}$$

which accounts for plasma shaping and the possible time dependence of the minor radius a.

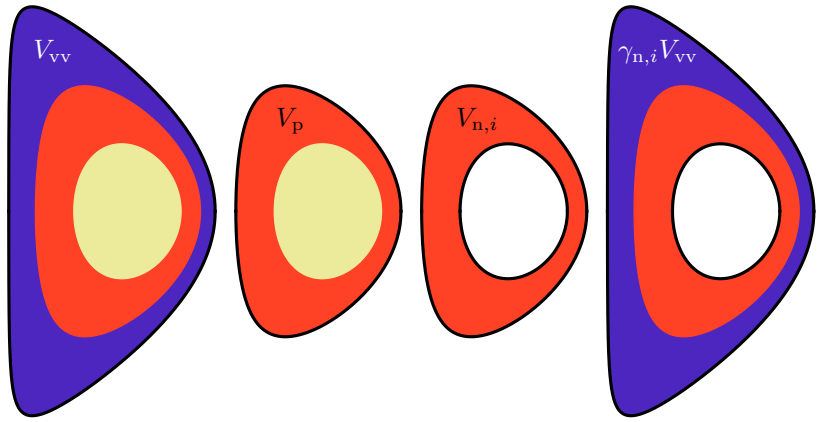

Figure 3.1: Illustration of volume partitioning for the two volume method. First is the full vacuum vessel volume V_{vv} (purple, red and light yellow), second is the plasma volume V_{p} (red and light yellow), third is the part of the volume $V_{\mathrm{n},i}$ where neutrals of ion species i remain (red), and last is the total volume $\gamma_{\mathrm{n},i}V_{\mathrm{vv}}$ where neutrals of ion species i remain (purple, red).

Due to neutral screening, neutral particles are not present in the full plasma volume, however, and the volume $V_{\mathrm{n},i}$ is the sub-volume where neutrals of ion species i remain, evaluated from the ionization mean free path. The ionization mean free path for ions of species i is evaluated from the thermal ion speed $v_{\mathrm{th},i} = \sqrt{2T_i/m_i}$, thermal electron density n_{th} and the ionization rate of the neutral $I_i^{(0)}$ as

$$\lambda_i = \frac{v_{\mathrm{th},i}}{n_{\mathrm{th}} I_i^{(0)}}. \tag{3.70}$$

Given the ionization mean free path, the volume where neutrals remain can be estimated by

$$\begin{aligned} V_{\mathrm{n},i}(t) = {} & 2\pi^2 R_0 \kappa \left[a(t)^2 - (a(t) - \lambda_i)^2\right] \\ & + 2\kappa\delta\,(8 - 3\pi)\left[a(t)^3 - \frac{(a(t) - \lambda_i)^3}{3}\right], \end{aligned} \tag{3.71}$$

where the first term is the full analytical expression for an elliptical plasma with elongation κ, and the second term is an approximation of the correction when accounting for the plasma triangularity δ.

Neutral particles are also present in the sub-volume of the vacuum vessel which does not contain plasma, and this sub-volume is denoted by $\gamma_{\mathrm{n},i}V_{\mathrm{vv}}$, where

$$\gamma_{\mathrm{n},i} = 1 - \frac{V_{\mathrm{p}} - V_{\mathrm{n},i}}{V_{\mathrm{vv}}}. \tag{3.72}$$

Inside the plasma, ions of species i and charge state j occupy the volume

$$\hat{V}_i^{(j)} = \begin{cases} V_{\mathrm{n},i} & \text{for } j = 0, \\ V_{\mathrm{p}} & \text{for } j \geq 1, \end{cases} \tag{3.73}$$

while inside the whole vacuum vessel, they occupy the volume

$$V_i^{(j)} = \begin{cases} \gamma_{\mathrm{n},i} V_{\mathrm{vv}} & \text{for } j = 0, \\ V_{\mathrm{p}} & \text{for } j \geq 1. \end{cases} \tag{3.74}$$

Notably, ionization of ions of species i and charge state j only occurs in the volume $\hat{V}_i^{(j)}$, while recombination occurs in the full plasma volume.

The ion density evolution is governed by

$$\begin{aligned} \frac{\partial n_i^{(j)}}{\partial t} = \frac{1}{V_i^{(j)}} \Big[& \hat{V}_i^{(j-1)} I_i^{(j-1)} n_{\mathrm{th}} n_i^{(j-1)} - \hat{V}_i^{(j)} I_i^{(j)} n_{\mathrm{th}} n_i^{(j)} \\ & + \hat{V}_i^{(j+1)} R_i^{(j+1)} n_{\mathrm{th}} n_i^{(j+1)} - \hat{V}_i^{(j)} R_i^{(j)} n_{\mathrm{th}} n_i^{(j)} \\ & + \hat{V}_{\mathrm{m}}^{(0)} n_{\mathrm{m}}^{(0)} A_{i,\mathrm{cx}}^{(j)} \Big] + S_i^{(j)}. \end{aligned} \tag{3.75}$$

Compared to the disruption model, equation (3.41), we account for neutral screening through the two-volume method by the inclusion of the factors $\hat{V}/V$ on the ionization, recombination and charge exchange terms. The term $\hat{V}_{\mathrm{m}}^{(0)} n_{\mathrm{m}}^{(0)} A_{i,\mathrm{cx}}^{(j)} / V_i^{(j)}$ represents the effect of charge exchange between neutrals of the main particle species and ions of other particle species, with the interaction factor

$$A_{i,\mathrm{cx}}^{(j)} = \begin{cases} -\sum_k \sum_l C_{ik}^{(l)} n_k^{(l)} & \text{for } i = m,\ j = 0,\ k \neq m, \\ +\sum_k \sum_l C_{ik}^{(l)} n_k^{(l)} & \text{for } i = m,\ j > 0,\ k \neq m, \\ C_{i\mathrm{m}}^{(j+1)} n_i^{(j+1)} - C_{i\mathrm{m}}^{(j)} n_i^{(j)} & \text{for } i \neq m, \end{cases} \tag{3.76}$$

where $C_{ik}^{(l)}$ denotes the charge exchange rate, which is also obtained from the ADAS database [44].

Additionally, we account for transport of ions and influx of neutral particles from fuelling or from wall sputtering, using the sink-source term $S_i^{(j)}$. For ions ($j \geq 1$),

$$S_i^{(j)} = -\frac{n_i^{(j)}}{\tau_i}, \tag{3.77}$$

while for neutrals ($j = 0$)

$$S_i^{(0)} = \frac{1}{V_i^{(0)}} \left[V_{\mathrm{p}} S_{i,\mathrm{s}} + \hat{V}_i^{(0)} S_{i,\mathrm{f}}^{(0)}(t) \right], \tag{3.78a}$$

where the first term represents wall sputtering and the second term plasma fuelling. Wall sputtering is a result of the ion bombardment of the wall due to incomplete ion confinement, and can have both chemical and physical causes.

Given the sputtering yield Y_{ik} of an ion of species i due to the incident species k, the total sputtering yield can be modelled as

$$S_{i,\mathrm{s}} = \sum_k \sum_{l \geq 1} Y_{ik} \frac{n_k^{(l)}}{\tau_k}. \tag{3.79}$$

When using the two-volume method, and accounting for particle confinement, for the evolution of the temperature, through the kinetic energy, equations (3.34) and (3.40) are modified according to

$$\frac{\partial W_{\mathrm{th}}}{\partial t} = \frac{j_\Omega}{B} E_\parallel - n_{\mathrm{th}} \sum_i \sum_{j=0}^{Z_i - 1} \frac{\hat{V}_i^{(j)}}{V_i^{(j)}} n_i^{(j)} L_i^{(j)} + \sum_i Q_{\mathrm{e}i} - \frac{W_{\mathrm{th}}}{\tau_{\mathrm{e}}}, \tag{3.80}$$

$$\frac{\partial W_i}{\partial t} = Q_{i\mathrm{e}} + \sum_k Q_{ik} - \frac{3}{2} \frac{\hat{V}_{\mathrm{m}}^{(0)}}{V_{\mathrm{p}}} n_{\mathrm{m}}^{(0)} \left(T_i - T_{\mathrm{m}}\right) C_{i,\mathrm{cx}}^{(1)} n_i^{(1)} - \frac{W_{\mathrm{i}}}{\tau_{\mathrm{i}}}. \tag{3.81}$$

Notably, the two-volume method is used for the inelastic atomic processes represented by $L_i^{(j)}$ and the charge exchange term, which is not included in the disruption model. In the charge exchange term, T_{m} is the temperature of the main ion species. Notably, the temperature of an ion species is the same for all charge states.

Runaway electrons

The low critical electric field, caused by the low prefill densities, is the main reason why runaway electrons risk being generated during tokamak start-up. For this reason, the main seed generation mechanism present would be Dreicer generation, and avalanche generation will also be significant. Hot-tail generation is not a concern during start-up, as it results from a rapid loss of thermal energy. Generation from Compton scattering and tritium beta decay could be present, but would be negligible compared to the Dreicer generation. For these reasons, the runaway electron density evolution is, in the start-up model, governed by

$$\frac{\partial n_{\mathrm{re}}}{\partial t} = \Gamma_{\mathrm{ava}} n_{\mathrm{re}} + \gamma_{\mathrm{D}} - \frac{n_{\mathrm{re}}}{\tau_{\mathrm{re}}}, \tag{3.82}$$

where we account for Dreicer and avalanche generation, as well as radial transport of runaway electrons due to incomplete particle confinement, as described above. The inclusion of runaway electrons in the start-up plasma evolution is an important aspect that sets the start-up model in paper A apart from other models for tokamak start-up, e.g. DYON [11, 50].

Chapter 4

Disruption mitigation optimization

During a disruption, the tokamak structure can generally be affected by electromechanical ($\boldsymbol{j} \times \boldsymbol{B}$) forces and high heat loads. These effects can cause torques and melting of plasma-facing components, respectively, and need to either be avoided or mitigated for successful tokamak reactors.

Electromechanical forces can be caused by eddy currents if the CQ is fast and halo currents if it is slow. Halo currents are currents circulating on open magnetic field lines that pass through both the plasma and the surrounding tokamak inner walls [12, 13]. If the halo currents are asymmetric, or spatially localized, they can produce large forces on local structures [13]. Asymmetries mainly arise during plasma vertical displacement events, which is why halo currents are mainly a concern for slow disruptions. If the current decays on a timescale faster than the plasma can be displaced, the risk of asymmetric halo currents is reduced [53]. Furthermore, the slower the current decay is, the longer time the halo currents have to load the surrounding structures with $\boldsymbol{j} \times \boldsymbol{B}$ forces.

On the other hand, if the disruption is too fast, eddy currents can be induced, which are currents circulating in plasma-facing conducting structures. When these eddy currents interact with the magnetic field, the resulting forces can cause localized torques on the plasma-facing conducting structures [12]. For disruption handling strategies, avoidance of electromechanical forces typically corresponds to having the duration of the CQ, commonly referred to as the CQ time, be within a certain interval, bounded from below to avoid forces from eddy currents, and from above to avoid forces from halo currents.

The main concern for high heat loads during the disruption comes from two sources – heat that is being transported and from a runaway current colliding with the tokamak wall. When the magnetic surfaces are broken up and the magnetic field lines are stochastic, the field lines can intercept the walls, causing heat to be transported into the wall [13]. How high the total heat load is depends on how much thermal energy is being carried by the transported charged particles of the plasma and the size of the area over which the energy is

spread out. The main strategy of minimizing heat loads due to heat transport is to increase radiative heat losses. Radiative heat losses are typically more uniformly spread than transported heat losses, and melting is mainly caused by relatively localized heat loads. Although there is a risk of melting caused by radiative losses, especially if they are not sufficiently uniform [54], the risk is lower than melting caused by transported heat losses.

Similarly, if a significant runaway current is generated, it can carry a significant fraction of the stored magnetic energy which could be deposited into the tokamak wall in a highly localized collision [5]. Since the criterion for runaway electron production is intricately linked to the electric field, as quantified by the Connor-Hastie field (see equation (2.2)), one strategy of runaway electron avoidance is to ensure a large critical electric field, mainly through increasing the density of the plasma since $E_c \propto n_e$. If a runaway seed is generated, the expulsion of these electrons from the plasma via perturbations of the magnetic field could prevent the development of a significant runaway current through avalanche.

Massive material injection (MMI) is a disruption mitigation strategy which can encompass mitigation with regard to electromechanical forces, transported heat loads and runaway electrons. The basic principle is to inject large amounts of cold and electrically neutral material into the hot plasma at the beginning of the disruption, with the type and amount of injected material being control parameters. The amount of material injected affects the temperature decay rate, and subsequently the CQ time, relevant for avoiding high electromechanical forces. Furthermore, injecting more material increases the plasma density, and subsequently the critical electric field, which in turn reduces the risk of runaway seed generation. Additionally, including atomic species with highly radiative properties reduces the heat loads due to transported heat losses. The most common MMI strategies involve injecting a combination of hydrogen isotopes, e.g. deuterium, to dilute the plasma, and noble gases, e.g. neon, to induce radiation, either in the form of gas injections or as shattered cryogenic pellets.

However, the different problems to be mitigated pose conflicting requirements on the injected material quantity and composition, especially since the runaway electron dynamics are not only affected through the critical electric field. If the TQ is fast, e.g. because of high radiative losses due to injected noble gases, there is a significant risk of hot-tail runaway seed generation [55]. Furthermore, the increased electron density can significantly amplify the avalanche generation ($\propto n_e$) due to the increased number of target electrons available for avalanching [38]. Care must therefore be taken in order to design the optimal disruption mitigation strategy, and disruption mitigation optimization is highly relevant during the development of future experimental devices such as SPARC and ITER.

4.1 Quantifying a disruption

To optimize disruption mitigation, the disruption evolution should be quantified by a scalar value that represents how successful the mitigation strategy is. Since

successful mitigation corresponds to low electromechanical forces from eddy and halo currents, as well as low heat loads from transported heat losses and runaway beam collisions with the wall, the scalar measure of the mitigation success can be obtained by quantifying and combining these, as has been done in papers B, C and D.

The CQ time can be estimated using [12]

$$\tau_{\mathrm{CQ}} = \frac{t_{I_\Omega = 0.2 I_\mathrm{p}^{t=0}} - t_{I_\Omega = 0.8 I_\mathrm{p}^{t=0}}}{0.6}, \tag{4.1}$$

i.e. through extrapolation based on the times at which the Ohmic current makes up 80 % and 20 % of the pre-disruption plasma current $I_\mathrm{p}^{t=0}$. The transported heat load can be quantified by the fraction of the initial plasma kinetic energy which has been lost from the plasma due to energy transport η_{tr}. Finally, the runaway current is commonly quantified either by its maximum value or by its value at the time when it reaches 95 % of the remaining total plasma current, and the two different options are compared in paper C.

Additionally, these papers have also accounted for the final Ohmic current I_Ω in the disruption optimization, to avoid uncertainties with regard to the current decay at times later than simulated. If the Ohmic current is large at the end of the simulation, the CQ duration is longer than ideal, and additionally, the CQ time estimation might not be accurate. Furthermore, a significant part of this current can still be transformed into runaway current.

To obtain one scalar value from the CQ time, transported heat load, runaway current and final Ohmic current, these representative figures of merit must be combined. For this we might use a weighted Euclidean norm of order p, such that the mitigation success is quantified by

$$\begin{aligned}\mathcal{L} = \big[&\big(c_{\tau_{\mathrm{CQ}}} f_{\tau_{\mathrm{CQ}}}(\tau_{\mathrm{CQ}})\big)^p + (c_{\eta_{\mathrm{tr}}} f_{\eta_{\mathrm{tr}}}(\eta_{\mathrm{tr}}))^p \\ &+ (c_{I_{\mathrm{re}}} f_{I_{\mathrm{re}}}(I_{\mathrm{re}}))^p + (c_{I_\Omega} f_{I_\Omega}(I_\Omega))^p\big]^{1/p},\end{aligned} \tag{4.2}$$

where the weights c and functions f are chosen to yield a representative quantification. For example, as the CQ time should not be minimized, but rather confined to a specified interval, the function $f_{\tau_{\mathrm{CQ}}}$ should be devised to "reward" CQ times within the interval and "penalize" CQ times outside of the interval.

4.2 Bayesian optimization

Bayesian optimization is a common type of black box optimization method, used to optimize functions where there is no mathematical expression relating the function argument to the function value. More specifically, black box optimization refers to optimization methods which do not depend on the structure of the function to be optimized. Instead, they map inputs to outputs and base their progression on the values of these input-output pairs. The core element of Bayesian optimization is the use of Bayes' theorem for determining the optimization progression. Bayes' theorem states that the conditional

probability of an event A given an event B is $p(A|B) = p(A)p(B|A)/p(B)$ [56], and provides a way of determining the probability of an event based on prior knowledge.

Fundamentally, Bayesian optimization uses Bayes' theorem applied to probability distributions for the *objective function* or *cost function* $\mathcal{L}$ which is to be optimized. In the context of Bayesian optimization, this means inferring the objective function value $\phi = \mathcal{L}(\boldsymbol{x})$ of all points $\boldsymbol{x}$ of a finite domain.

Bayes' theorem for probability distributions of the objective function at a specific point $\boldsymbol{x}$ is

$$p(\phi|\boldsymbol{x}, y) = \frac{p(\phi|\boldsymbol{x})p(y|\boldsymbol{x}, \phi)}{p(y|\boldsymbol{x})}, \tag{4.3}$$

where the variable y is the measurement received when observing the objective function $\mathcal{L}$ at $\boldsymbol{x}$ [57]. Here, $p(\phi|\boldsymbol{x})$ is called the prior distribution, and describes our prior knowledge of how plausible different function values ϕ are, before observing any data. The likelihood function $p(y|\boldsymbol{x}, \phi)$ describes the likelihood of getting the measurement y as a function of $\phi = \mathcal{L}(\boldsymbol{x})$ when making an observation of the objective function at $\boldsymbol{x}$. These two probability distributions determine the posterior distribution function $p(\phi|\boldsymbol{x}, y)$, which describes the probability distribution over the objective function value ϕ given $\boldsymbol{x}$ and the measurement y observed at $\boldsymbol{x}$. The denominator of (4.3) is called evidence and ensures the normalization of the posterior,

$$p(y|\boldsymbol{x}) = \int p(\phi|\boldsymbol{x})p(y|\boldsymbol{x}, \phi)\mathrm{d}\phi. \tag{4.4}$$

This can be extended to find the posterior distribution function of the entire function $\mathcal{L}(\boldsymbol{x})$

$$p(\phi(\boldsymbol{x})|\mathcal{D}) = \frac{p(\phi(\boldsymbol{x})|\boldsymbol{x})p(\mathcal{D}|\boldsymbol{x}, \phi(\boldsymbol{x}))}{p(\mathcal{D})}, \tag{4.5}$$

where $\phi(\boldsymbol{x})$ represents the actual function values in a subset to the domain of $\mathcal{L}$. Here, the knowledge we have about the objective function is collected in the data set $\mathcal{D} = \{(\boldsymbol{x}_i, y_i)\}_{i=1}^{N}$, which consists of N observation pairs – measurements y_i observed at position $\boldsymbol{x}_i$.

In order to use (4.5) to make viable predictions for the objective function, an assumption of the nature of the probability distribution of $\phi(\boldsymbol{x})$ is needed. In Bayesian optimization, it is assumed that the objective function value at every point of the function domain is a random variable. Since the domain is continuous, this is equivalent to having an infinite collection of random variables, which is the definition of a *stochastic process* [57]. An especially common stochastic process used for Bayesian optimization is the Gaussian process (GP), in which the random variables are distributed according to multivariate Gaussian distributions. A GP on the objective function $\mathcal{L}(\boldsymbol{x})$ is specified by a mean function $\mu(\boldsymbol{x}) = \mathbb{E}[\phi|\boldsymbol{x}]$, which determines the expected function value $\phi = \mathcal{L}(\boldsymbol{x})$ at any $\boldsymbol{x}$, and a covariance function, or kernel, $K(\boldsymbol{x}, \boldsymbol{x}')$, which measures the correlation between ϕ for points $\boldsymbol{x}$ and $\boldsymbol{x}'$ [57], and determines the variance $\sigma(\boldsymbol{x})^2$ of the GP. The mean function $\mu(\boldsymbol{x})$ and

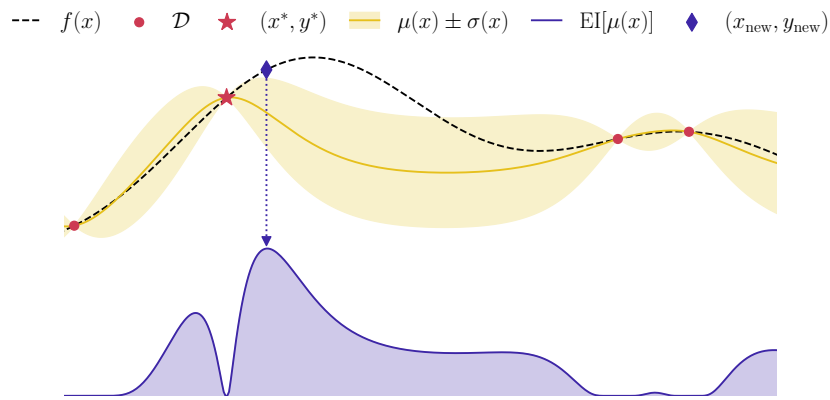

Figure 4.1: Illustration of the key elements of Bayesian optimization. The objective function is plotted in black (dashed) and the samples included in the dataset $\mathcal{D}$ are marked by red circles, except for the current maximum y^* which is marked by a star. The mean function $\mu(x)$ with one standard deviation, determined by the kernel, is plotted in yellow and the EI acquisition function is plotted in purple, with the suggested next sample indicated by a purple diamond.

standard deviation $\sigma(\boldsymbol{x})$ are illustrated for an example Bayesian optimization in figure 4.1.

The covariance function $K(x, x')$ can be defined in different ways, and therefore needs to be specified before a GP can be used. One widely used kernel is the Matérn kernel, which determines the covariance between two points based on the Euclidean distance between them – points that are closer to each other in the function domain are assumed to be more strongly correlated [57]. The exact mathematical form of the Matérn kernel depends on a "smoothness" parameter ν, which determines how smooth the functions drawn from the GP should be. In turn, this impacts the smoothness of the mean function determining the expected values of the objective function. The suitable choice of ν depends on the expected function behaviour of the objective function. More specifically, the sample paths obtained from a Matérn kernel based GP with smoothness parameter ν is $\lceil \nu \rceil - 1$ times continuously differentiable, i.e. once differentiable if $\nu = 3/2$ and twice if $\nu = 5/2$.

The expected function behaviour that is obtained from the GP is used to inform the optimizer about which point $\boldsymbol{x}$ to sample next, based on some kind of strategy. This strategy for determining which point to sample next, given the expected function behaviour, is called the *acquisition function*, and its purpose is to determine which new point in the domain would yield most information regarding the position of the optimum of the objective function. There are several kinds of acquisition functions, and a commonly used one is the expected improvement (EI) acquisition function. Using EI, the new points

are selected based on the maximum of the expected improvement

$$\boldsymbol{x}_{\text{new}} = \arg\max_{\boldsymbol{x}} \left[\mathbb{E}[I(\boldsymbol{x}, y^*)]\right] = \arg\max_{\boldsymbol{x}} \left[\int I(\boldsymbol{x}, \phi, y^*) p(\phi|\boldsymbol{x}, \mathcal{D}) \mathrm{d}\phi\right], \quad (4.6)$$

where

$$I(\boldsymbol{x}, \phi, y^*) = \begin{cases} \max(\phi - y^*, 0) & \text{(for maximization)}, \\ \max(y^* - \phi, 0) & \text{(for minimization)}, \end{cases} \quad (4.7)$$

is a measure of the improvement [58]. Here, y^* is the optimal objective function value encountered so far.

As with many stochastic optimization algorithms, the concepts of exploration and exploitation are relevant [57]. An optimizer which favours exploitation prefers to look for the optimum close to the best candidate for an optimum found so far. On the other hand, if exploration is favoured, the optimizer prefers to look for the optimum in regions far from other observations where the uncertainties are large. In Bayesian optimization, the exploration–exploitation trade-off is modelled in the acquisition function. This trade-off is not parametrized in the original EI acquisition function, but the acquisition function can be modified to account for it. In the Bayesian-Optimization Python module [59], the EI has been modified by introducing an exploration-exploitation trade-off parameter, ξ, to (4.6) according to

$$I(\boldsymbol{x}, \phi, y^*) = \max(\phi - y^*,\ 0) \rightarrow \max(\phi - y^* - \xi,\ 0), \quad (4.8)$$

where exploration increases with ξ.

To summarize Bayesian optimization as applied to disruption mitigation, the method starts with a GP prior, determined by the initial knowledge and assumptions we have made about the disruption cost function $\mathcal{L}(\tau_{\text{CQ}},\ \eta_{\text{tr}},\ I_{\text{re}},\ I_{\Omega})$. By using the data set $\mathcal{D}$ of already performed disruption simulations, a likelihood distribution function is obtained which, together with the GP prior, yields a GP posterior for the disruption cost function. This GP posterior is then used by the acquisition function to determine the most promising new position, $\boldsymbol{x}_{\text{new}}$, in the mitigation parameter space to perform a new simulation in order to improve the current optimum, yielding a new data point $(\boldsymbol{x}_{\text{new}}, y_{\text{new}})$. Bayesian optimization is therefore an iterative process, in which each new disruption simulation, with mitigation parameter chosen based on the acquisition function's proposition, can be added to the data set of disruption simulations $\mathcal{D}$ and the optimization can be repeated with the updated disruption simulation data set $\mathcal{D}$.

The advantage of using Bayesian optimization is the combination of obtaining the optimum and an estimation for the cost function in the full optimization domain. Hence, through Bayesian optimization, exploration of the relevant domain, especially around the optimal areas, can be obtained with relatively few samples needed, as opposed to a grid search. For these reasons, Bayesian optimization was used to optimize disruption mitigation in papers B, C and D.

Chapter 5

Summary and outlook

Runaway electrons will be a severe problem for future tokamaks with high plasma currents, specifically during start-up and disruptions. Developing strategies for runaway electron mitigation and avoidance in future devices such as ITER and SPARC is an active field within fusion research. Due to the serious risks runaway electrons pose to these devices, and the fact that relevant conditions cannot be accessed in current experiments, numerical exploration of the operational regimes are required to inform the strategy development. As the runaway electron evolution is intricately connected to the overall plasma evolution, it is essential that the numerical plasma models used for studying tokamak start-up and disruptions are accurate. In such modelling efforts, aside from the runaway electrons, the electric field, temperature and other particle populations need to be considered, and effects such as transport of particles and energy, radiation and inelastic atomic processes need to be accounted for. With appropriate plasma models in place, it is possible to comprehensively study different mitigation strategies through explorative optimization. Having an idea about the optimal mitigation strategies before the start of operation could help guide and accelerate the experimental advancement.

This thesis focuses on the development of accurate plasma models for studying runaway electrons during tokamak start-up and disruptions, as well as using such plasma models for optimizing disruption mitigation. The findings of the appended papers are highlighted and summarized here, and possible directions for future research based on this work are also presented.

5.1 Summary of papers

The research presented in the appended papers regard plasma modelling and optimization of disruption mitigation. Paper A presents a tool developed to study runaway electrons during tokamak start-up, while papers B and D describe disruption mitigation optimization of ITER and SPARC, respectively. In paper C, fluid or kinetic modelling of the runaway seed generation are compared, and the exploration of different disruption scenarios is realized through optimization of disruption mitigation in ITER.

In paper A, the developed start-up simulation tool STREAM is presented and used for studying under which circumstances significant runaway generation is present or suppressed. The underlying model used for governing the start-up plasma evolution accounts for the externally applied electric field, incomplete particle confinement and neutral screening effects, and is described in more detail in section 3.2. STREAM is benchmarked against the start-up simulation tool DYON [11, 50], and the two codes are found to be in good agreement.

To investigate runaway dynamics during start-up, a simplified ITER first plasma scenario is studied. The start-up scenario assumed a pure deuterium plasma, with constant loop voltage and plasma volume evolution. It is found that for the planned prefill pressure of the ITER first plasma scenario, no significant runaway current is formed. The reason for this is that the transport losses dominate the runaway evolution during the period of the start-up when the electric field is sufficiently strong for runaways to be generated. However, if the prefill pressure is reduced by a factor of 10, the plasma current is soon dominated by runaway electrons, as the electric field is sufficiently strong for runaway generation, even after the formation of closed magnetic surfaces.

The main generation mechanism for this case is Dreicer generation, and not avalanche, which is usually the dominant generation mechanism in disruption scenarios with significant runaway currents. For this scenario, with constant loop-voltage and low prefill pressure, a high electric field to Dreicer field ratio is maintained throughout the start-up, enabling significant Dreicer generation. In contrast, during disruptions, a high E/E_D is usually only maintained for brief periods of the thermal quench. This can still be sufficient for Dreicer generation to form a runaway seed which can be exponentiated through avalanche multiplication. Notably, the ratio E/E_D could be used as a more representative quantity for start-up runaway generation than the ratio E/E_c, as the former determines the Dreicer generation, while the latter sets the avalanche generation.

As a low prefill pressure results in significant runaway formation, suppressing the runaway electron beam could be achieved by increasing the plasma density through fuelling. This is also studied in paper A, starting from the same prefill pressure which generated a significant runaway current, but employing plasma fuelling starting at different times during the start-up evolution. If the plasma fuelling is employed too early during the start-up, burn-through could fail, but employed too late, a significant runaway population can form, reducing the effectiveness of the plasma fuelling for runaway suppression. The early use of plasma fuelling for effective suppression of runaway beam formation is supported by results of the paper. The temperature ramp-up is however also more efficient for the early fuelling scenarios considered, as the electric field can more effectively heat the plasma through ohmic heating if the ohmic component of the plasma current is sufficiently large. This signified that for start-up scenarios with a large enough runaway population, the burn-through can fail to due insufficient ohmic heating.

We study disruption mitigation optimization for an ITER deuterium-tritium H-mode plasma **in paper B**, using the disruption simulation tool DREAM [40]. More specifically, the densities of the injected deuterium and neon during

massive material injection are optimized. To begin with, only the magnitudes of the injected densities are optimized, with the density distribution being set as spatially uniform. Subsequently, we also optimize the radial distribution with regard to favouring inward or outward peaking. The disruption mitigation is quantified by the runaway current, transported fraction of the heat loss and the current quench time, which are combined to obtain one scalar value.

All optima found corresponded to runaway currents of several mega-amperes. When isolating the dependence of the injected density magnitudes, i.e. when the radial profiles are uniform, it is found that when high amounts of deuterium are injected, the runaway dynamics are significantly influenced by deuterium recombination. With high amounts of injected deuterium, the temperature decays at a faster rate, increasing the deuterium recombination. Deuterium recombination decreases the free-to-total electron density ratio, which increases the avalanching (see equation (2.35)). However, due to the high deuterium density, and subsequently high free electron density (in absolute terms), the Connor-Hastie electric field is relatively high at the end of the disruption. This results in a decaying runaway current, after the current peaks (still at several mega-amperes, as noted earlier), rather than the formation of a steady runaway plateau. With lower deuterium densities, the plateau phase is more pronounced, as the runaway current is kept at a quite steady level.

With increasing neon content, the radiative heat losses are increased, which affects both the runaway dynamics and the transported fraction of the heat loss. The runaway dynamics are affected through the temperature balance, as the first thermal equilibrium after the injected material has been introduced occurs at a lower temperature for higher radiative heat losses. A lower equilibrium temperature in turn correlates to a higher electric field to Connor-Hastie field ratio (E/E_c), corresponding to more efficient avalanching. With high radiative heat losses, the transported fraction of the heat losses are naturally reduced. However, a high neon density is not necessarily sufficient for acceptable levels of the transported fraction of the heat losses – sufficient deuterium densities are required as well, to dilute the plasma.

When investigating the optimal radial distributions for the injected deuterium and neon densities, it is found that an edge-peaked neon density is favourable. An edge-peaked radial distribution can allow for sufficient radiative heat losses at the edge, while limiting the effect of the neon on the runaway dynamics close to the core, where runaway generation is most significant. Furthermore, a moderately uniform radial distribution for the deuterium density is most advantageous. More specifically, the edge deuterium density is less important for the runaway evolution, meaning that the essential consideration for the deuterium density is that it should be at an adequate level in the core (i.e. not too high nor too low).

Disruption mitigation optimization is further studied **in paper C**, however in this paper, the main objective is to compare fluid and kinetic modelling of the runaway electron seed generation. With this goal in mind, kinetic source terms are derived for the generation of energetic electrons from tritium beta decay and Compton scattering. The same ITER-like tokamak set-up is used as in paper B, but a pure deuterium scenario is studied, in addition to a

deuterium-tritium plasma scenario. Furthermore, only spatially homogeneous density profiles of the injected material are considered.

The comparison of fluid and kinetic modelling of the runaway seed generation showed that hot-tail generation deviated the most. The hot-tail generation is naturally included in the momentum space particle flux determined by the kinetic equation (3.21), while the fluid model uses the analytical formula (2.25). To derive this analytical formula, spatial transport effects were neglected to obtain an estimation of the distribution function based on the evolution of the fluid plasma parameters. Thus, radial transport due to magnetic perturbations is not considered in the evolution of the distribution, which results in an overestimation of the hot-tail generation rate. During the TQ, part of the hot-tail is lost due to the broken flux surfaces, which is accounted for in the kinetic treatment of the hot-tail generation, but not in the fluid one.

This model discrepancy is not as prominent for the deuterium-tritium scenario, however, due to the inclusion of the activated sources. Tritium beta decay and Compton scattering generates energetic electrons with momenta both above and below the critical one, so that the distribution function for energetic electrons is not depleted by radial transport. Instead, it reaches a level where the transport losses are balanced by the generation of new energetic electrons from tritium beta decay and Compton scattering. Even though some of these electrons are not initially generated above the critical momentum, they can run away at a later point, either through momentum space diffusion or through a rapid decrease of the critical momentum. This effect is not considered in the fluid models for the activated runaway generation mechanisms. However, the overestimation of the fluid hot-tail model is found to compensate for this, such that the fluid and kinetic simulations predicted similar runaway dynamics.

It is found that it is not possible to simultaneously achieve acceptable levels of the runaway current, transported heat fraction and current quench time in deuterium-tritium plasmas. Acceptable levels of the transported heat fraction or the current quench time are always correlated with runaway currents of several mega-amperes, which is in agreement with the findings of paper B. For the pure deuterium plasmas however, successful disruption mitigation is predicted to be possible using the more accurate kinetic simulations, for high injected deuterium densities and moderate neon densities.

In paper D, disruption mitigation optimization is performed for SPARC. For the massive material injection, deuterium is combined not only with neon, but also with argon and helium, to investigate how different choices of noble gas affects the disruption evolution. As in paper C, radially uniform density profiles are used for the injected material. We consider the SPARC primary reference discharge during deuterium-tritium operation. Additionally, the same initial set-up is also used for a pure-deuterium plasma scenario. For the pure deuterium plasma, we consider both the artificial case of no Compton scattering, as well as Compton scattering caused by photons resulting from neutrons of the deuterium-deuterium fusion reaction. Based on the results of paper C, the runaway seed generation is treated kinetically, for more accurate results.

For all scenarios considered (i.e. for pure deuterium plasmas with and without accounting for Compton scattering, as well as for deuterium-tritium

plasmas) successful disruption mitigation is found to be possible with injection of deuterium and neon. However, as the activated sources play a greater role in the dynamics, the area in the injected material density space corresponding to successful mitigation is reduced. In deuterium-tritium plasmas, it is found to only be possible for the highest deuterium densities considered. The explanation for why successful mitigation is possible in the SPARC primary reference discharge, but not in activated scenarios of ITER, is the lower plasma current planned for SPARC. In SPARC, the plasma current will be 8.7 MA, compared to the 15 MA of ITER's H-mode scenario. Since the avalanche generation is exponentially sensitive to the magnitude of the plasma current, the ITER scenarios yield more runaway current.

It is noted that there exists a trade-off between minimizing the runaway current and the transported fraction of the heat loss, in agreement with the findings of paper B and C. In general, the lowest runaway currents correspond to low neon densities, while the lowest transported heat fractions correspond to high neon densities. As previously noted, high neon densities cause high radiative heat losses, which reduces the transported fraction of the heat loss, but it also leads to increased avalanching. Furthermore, the trade-off between minimizing the runaway current and the transported heat fraction is found to be less favourable for injection of helium or argon, compared to neon. Injection of helium results in less effective heat losses through radiation, while injection of argon enhanced the avalanche significantly, due to its high atomic number, resulting in a high total electron density.

5.2 Outlook

As electron runaway is inherently a momentum space phenomenon, certain situations require kinetic modelling for sufficient accuracy. One of the main findings of this thesis is the significant impact which a kinetic treatment of the runaway seed generation had on the runaway evolution, illustrating the need for kinetic modelling of runaway electron dynamics. However, in all the work included in this thesis, the avalanche generation is accounted for using a fluid description. The reduced kinetic model, which is described in section 3.1, can reliably model seed generation due to the relatively low energies of the electrons involved in the primary generation. Avalanche generation, on the other hand, involves electrons of relativistic momenta, meaning that this reduced model can not be used to describe secondary generation. For a kinetic treatment of the avalanche generation, the runaway electrons, rather than the superthermal electrons, need to be evolved kinetically. There are avalanche operators of different levels of sophistication that can be used. An approximate model was developed by Rosenbluth and Putvinski [19], which is based on the assumption that all runaway electrons involved in the avalanche generation have essentially infinite energy and travel parallel to the magnetic field lines, yielding a spectrum of secondary runaways. Due to this assumption, however, the spectrum of the generated secondary runaways extends to infinite energies, which is not physical. An avalanche operator accounting for the

energy distribution of the incoming runaway electrons was derived by Chiu et al. [60]. As the energy distribution of the incoming runaway electrons is considered, the energies obtained by the secondary runaways are reasonably limited. One of the most accurate avalanche operators was derived from the Boltzmann operator [61], which additionally considers the distribution in pitch angle and conserves particle number and momentum. Using any of these three avalanche operators would improve the accuracy of the runaway electron evolution. However, since using these avalanche operators requires resolving the momentum and pitch angle distribution of the runaway population, simulations with kinetic avalanche generation would be computationally more expensive. Using kinetic avalanche generation during optimization might therefore not be beneficial enough to motivate the higher computational cost. Instead, fluid avalanche generation could be used for the sampling during the optimization, and kinetic avalanche for a number of selected samples, to validate the results of the optimization.

To further improve the start-up model for studying runaway electrons, STREAM could be extended to include both a radial dependence and the possibility to use kinetic plasma models. Compared to the kinetic model used to describe disruptions, it is mainly the effect of transport on the distribution function that would require modification. Specifically, the sound speed should be exchanged for the parallel velocity component, for a more accurate description of the parallel transport.

To include the radial dimension in the start-up model, it would no longer be desirable to use the two-volume method to account for neutral screening effects. A consequence of neutral screening is that neutrals and charged particles occupy different subsets of the vacuum vessel volume, which affects particle and energy balance. The two-volume method solves this problem by weighting the terms in the balance equations differently (see section 3.2 for more details). Having a radial dimension would instead mean that the different subvolumes would be spatially resolved. This would require modelling not only the plasma, but the full vacuum vessel, to fully account for the neutral screening effects. This could perhaps be done similarly to the 1D diffusion model used in Ref. [62].

Finally, the disruption models used for the optimization could be further improved with regard to the MMI model, which is currently relatively simplistic. In its current form, the deposition of the neutral material is assumed to be instantaneous and uniformly distributed. In reality, the material would either be injected in the form of shattered pellets or as gas, which both would require time to reach the plasma core, from the edge. This would mean that, radially, the effect of the neutral material would not affect the plasma synchronously, which could impact the plasma evolution. There are models for radial transport of neutrals and ions in DREAM, which could be employed during optimization to study the effect of the temporal and spatial dependence of the MMI. These models are not self-consistent, however, and the transport coefficients need to be known and prescribed. Still, using such a model and employing suitable transport coefficients would improve the accuracy and predictive capability of the simulations used during the optimization.

References

[1] *Energy use per person vs. GDP per capita.* [Online]. Available: https://ourworldindata.org/grapher/energy-use-per-person-vs-gdp-per-capita?time=2023 (visited on 05/02/2025).

[2] J. P. Freidberg, *Plasma physics and fusion energy*, 1. paperback ed. Cambridge University Press, 2008, ISBN: 9780521733175.

[3] *Advantages of fusion.* [Online]. Available: http://www.iter.org/sci/fusion (visited on 10/02/2023).

[4] J. Wesson, *Tokamaks*, 4. ed. Oxford University Press, 2011, ISBN: 9780199592234.

[5] B. N. Breizman, P. Aleynikov, E. M. Hollmann and M. Lehnen, 'Physics of runaway electrons in tokamaks,' *Nuclear Fusion*, vol. 59, no. 8, p. 083 001, 2019. DOI: 10.1088/1741-4326/ab1822.

[6] F. F. Chen, *Introduction to Plasma Physics and Controlled Fusion*, 3rd ed. Springer, 2018, ISBN: 9783319793917.

[7] P. Helander and D. J. Sigmar, *Collisional transport in magnetized plasmas* (Cambridge monographs on plasma physics), Digitally printed 1st pbk. version. Cambridge University Press, 2005, ISBN: 9780521020985.

[8] B. J. Braams and C. F. F. Karney, 'Differential form of the collision integral for a relativistic plasma,' *Phys. Rev. Lett.*, vol. 59, p. 1817, 1987. DOI: 10.1103/PhysRevLett.59.1817.

[9] R. L. Miller, M. S. Chu, J. M. Greene, Y. R. Lin-Liu and R. E. Waltz, 'Noncircular, finite aspect ratio, local equilibrium model,' *Physics of Plasmas*, vol. 5, no. 4, p. 973, 1998. DOI: 10.1063/1.872666.

[10] D. Mueller, 'The physics of tokamak start-up,' *Physics of Plasmas*, vol. 20, no. 5, p. 058 101, 2013. DOI: 10.1063/1.4804416.

[11] H.-T. Kim, W. Fundamenski, A. C. C. Sips and EFDA-JET Contributors, 'Enhancement of plasma burn-through simulation and validation in JET,' *Nuclear Fusion*, vol. 52, no. 10, p. 103 016, 2012. DOI: 10.1088/0029-5515/52/10/103016.

[12] T. C. Hender *et al.*, 'Chapter 3: MHD stability, operational limits and disruptions,' *Nuclear Fusion*, vol. 47, no. 6, S128, 2007. DOI: 10.1088/0029-5515/47/6/S03.

[13] A. H. Boozer, 'Theory of tokamak disruptions,' *Physics of Plasmas*, vol. 19, no. 5, p. 058 101, 2012. DOI: 10.1063/1.3703327.

[14] R. Sweeney *et al.*, 'MHD stability and disruptions in the SPARC tokamak,' *Journal of Plasma Physics*, vol. 86, no. 5, p. 865 860 507, 2020. DOI: 10.1017/S0022377820001129.

[15] E. M. Hollmann *et al.*, 'Status of research toward the ITER disruption mitigation system,' *Physics of Plasmas*, vol. 22, no. 2, p. 021 802, 2015. DOI: 10.1063/1.4901251.

[16] H. Knoepfel and D. A. Spong, 'Runaway electrons in toroidal discharges,' *Nuclear Fusion*, vol. 19, no. 6, p. 785, 1979. DOI: 10.1088/0029-5515/19/6/008.

[17] C. Reux *et al.*, 'Runaway electron beam generation and mitigation during disruptions at JET-ILW,' *Nuclear Fusion*, vol. 55, no. 9, p. 093 013, 2015. DOI: 10.1088/0029-5515/55/9/093013.

[18] M. Lehnen *et al.*, 'Disruptions in ITER and strategies for their control and mitigation,' *Journal of Nuclear Materials*, vol. 463, p. 39, 2015. DOI: https://doi.org/10.1016/j.jnucmat.2014.10.075.

[19] M. N. Rosenbluth and S. V. Putvinski, 'Theory for avalanche of runaway electrons in tokamaks,' *Nuclear Fusion*, vol. 37, no. 10, p. 1355, 1997. DOI: 10.1088/0029-5515/37/10/I03.

[20] C. T. R. Wilson, 'The acceleration of β-particles in strong electric fields such as those of thunderclouds,' *Mathematical Proceedings of the Cambridge Philosophical Society*, vol. 22, no. 4, p. 534, 1925. DOI: 10.1017/S0305004100003236.

[21] A. S. Eddington, 'The source of stellar energy,' *Nature*, vol. 117, no. 2948, p. 25, 1926. DOI: 10.1038/117025a0.

[22] G. D. Holman, 'Acceleration of runaway electrons and joule heating in solar flares,' *Symposium - International Astronomical Union*, vol. 107, p. 191, 1985. DOI: 10.1017/S0074180900075616.

[23] J. W. Connor and R. J. Hastie, 'Relativistic limitations on runaway electrons,' *Nuclear Fusion*, vol. 15, no. 3, p. 415, 1975. DOI: 10.1088/0029-5515/15/3/007.

[24] L. Hesslow, O. Embréus, G. J. Wilkie, G. Papp and T. Fülöp, 'Effect of partially ionized impurities and radiation on the effective critical electric field for runaway generation,' *Plasma Physics and Controlled Fusion*, vol. 60, no. 7, p. 074 010, 2018. DOI: 10.1088/1361-6587/aac33e.

[25] R. Jayakumar, H. H. Fleischmann and S. J. Zweben, 'Collisional avalanche exponentiation of runaway electrons in electrified plasmas,' *Physics Letters A*, vol. 172, no. 6, p. 447, 1993. DOI: https://doi.org/10.1016/0375-9601(93)90237-T.

[26] L. Hesslow, L. Unnerfelt, O. Vallhagen, O. Embreus, M. Hoppe, G. Papp and T. Fülöp, 'Evaluation of the Dreicer runaway generation rate in the presence of high-Z impurities using a neural network,' *Journal of Plasma Physics*, vol. 85, no. 6, p. 475 850 601, 2019. DOI: 10.1017/S0022377819000874.

[27] Y. Lee, P. Aleynikov, P. C. de Vries, H.-T. Kim, J. Lee, M. Hoppe, J.-K. Park, G. J. Choi, J. Gwak and Y.-S. Na, 'Binary nature of collisions facilitates runaway electron generation in weakly ionized plasmas,' *Phys. Rev. Lett.*, vol. 133, p. 175 102, 2024. DOI: 10.1103/PhysRevLett.133.175102.

[28] P. Helander, H. Smith, T. Fülöp and L.-G. Eriksson, 'Electron kinetics in a cooling plasma,' *Physics of Plasmas*, vol. 11, no. 12, p. 5704, 2004. DOI: 10.1063/1.1812759.

[29] R. W. Harvey, V. S. Chan, S. C. Chiu, T. E. Evans, M. N. Rosenbluth and D. G. Whyte, 'Runaway electron production in DIII-D killer pellet experiments, calculated with the CQL3D/KPRAD model,' *Physics of Plasmas*, vol. 7, no. 11, p. 4590, 2000. DOI: 10.1063/1.1312816.

[30] H. Smith, P. Helander, L.-G. Eriksson and T. Fülöp, 'Runaway electron generation in a cooling plasma,' *Physics of Plasmas*, vol. 12, no. 12, p. 122 505, 2005. DOI: 10.1063/1.2148966.

[31] H. M. Smith and E. Verwichte, 'Hot tail runaway electron generation in tokamak disruptions,' *Physics of Plasmas*, vol. 15, no. 7, p. 072 502, 2008. DOI: 10.1063/1.2949692.

[32] L. Hesslow, O. Embréus, M. Hoppe, T. C. DuBois, G. Papp, M. Rahm and T. Fülöp, 'Generalized collision operator for fast electrons interacting with partially ionized impurities,' *Journal of Plasma Physics*, vol. 84, no. 6, p. 905 840 605, 2018. DOI: 10.1017/S0022377818001113.

[33] K. S. Krane, *Introductory Nuclear Physics*. John Wiley & Sons, 1988.

[34] E. Fermi, 'Versuch einer Theorie der β-Strahlen. I,' *Zeitschrift für Physik*, vol. 88, no. 3-4, p. 161, 1934, ISSN: 1434-6001, 1434-601X. DOI: 10.1007/BF01351864.

[35] J. R. Martín-Solís, A. Loarte and M. Lehnen, 'Formation and termination of runaway beams in ITER disruptions,' *Nuclear Fusion*, vol. 57, no. 6, p. 066 025, 2017. DOI: 10.1088/1741-4326/aa6939.

[36] O. Vallhagen, O. Embréus, I. Pusztai, L. Hesslow and T. Fülöp, 'Runaway dynamics in the DT phase of ITER operations in the presence of massive material injection,' *Journal of Plasma Physics*, vol. 86, no. 4, p. 475 860 401, 2020. DOI: 10.1017/S0022377820000859.

[37] O. Klein and Y. Nishina, 'Über die streuung von strahlung durch freie elektronen nach der neuen relativistischen quantendynamik von Dirac,' *Zeitschrift für Physik*, vol. 52, no. 11-12, p. 853, 1929. DOI: 10.1007/BF01366453.

[38] L. Hesslow, O. Embréus, O. Vallhagen and T. Fülöp, 'Influence of massive material injection on avalanche runaway generation during tokamak disruptions,' *Nuclear Fusion*, vol. 59, no. 8, p. 084 004, 2019. DOI: 10.1088/1741-4326/ab26c2.

[39] B. Buchholz, *Calculation of the runaway electron current in tokamak disruptions*, 2023. arXiv: 2309.10827 [physics.plasm-ph].

[40] M. Hoppe, O. Embréus and T. Fülöp, 'DREAM: A fluid-kinetic framework for tokamak disruption runaway electron simulations,' *Computer Physics Communications*, vol. 268, p. 108 098, 2021, ISSN: 0010-4655. DOI: 10.1016/j.cpc.2021.108098.

[41] A. Redl, C. Angioni, E. Belli, O. Sauter and ASDEX Upgrade Team and EUROfusion MST1 Team, 'A new set of analytical formulae for the computation of the bootstrap current and the neoclassical conductivity in tokamaks,' *Physics of Plasmas*, vol. 28, no. 2, p. 022 502, 2021. DOI: 10.1063/5.0012664.

[42] A. Kramida, Y. Ralchenko, J. Reader and NIST ASD Team, *NIST atomic spectra database, (ver. 5.8)*, National Institute of Standards and Technology, Gaithersburg, MD, 2021. DOI: 10.18434/T4W30F. [Online]. Available: https://physics.nist.gov/asd.

[43] D. Reiter, *The data file AMJUEL: Additional atomic and molecular data for EIRENE*, 2020. [Online]. Available: https://www.eirene.de/Documentation/amjuel.pdf.

[44] *OPEN-ADAS: Atomic data and analysis structure*, University of Strathclyde. [Online]. Available: https://open.adas.ac.uk/.

[45] N. A. Garland, H.-K. Chung, C. J. Fontes, M. C. Zammit, J. Colgan, T. Elder, C. J. McDevitt, T. M. Wildey and X.-Z. Tang, 'Impact of a minority relativistic electron tail interacting with a thermal plasma containing high-atomic-number impurities,' *Physics of Plasmas*, vol. 27, no. 4, p. 040 702, 2020. DOI: 10.1063/5.0003638.

[46] A. B. Rechester and M. N. Rosenbluth, 'Electron heat transport in a tokamak with destroyed magnetic surfaces,' *Phys. Rev. Lett.*, vol. 40, p. 38, 1978. DOI: 10.1103/PhysRevLett.40.38.

[47] K. Särkimäki, O. Embreus, E. Nardon, T. Fülöp and JET contributors, 'Assessing energy dependence of the transport of relativistic electrons in perturbed magnetic fields with orbit-following simulations,' *Nuclear Fusion*, vol. 60, no. 12, p. 126 050, 2020. DOI: 10.1088/1741-4326/abb9e9.

[48] P. Svensson, O. Embreus, S. L. Newton, K. Särkimäki, O. Vallhagen and T. Fülöp, 'Effects of magnetic perturbations and radiation on the runaway avalanche,' *Journal of Plasma Physics*, vol. 87, no. 2, p. 905 870 207, 2021. DOI: 10.1017/S0022377820001592.

[49] A. B. Mineev, V. A. Belyakov, Y. V. Gribov, A. A. Kavin, K. M. Lobanov, A. V. Belov, E. A. Lamzin and S. E. Sytchevsky, 'Study of ITER first plasma initiation using a 3d electromagnetic model,' in *Proceedings of the 25th IAEA Fusion Energy Conference*, 2014.

[50] H.-T. Kim, A. Mineev, D. Ricci, J.-W. Lee, Y.-S. Na, ITPA-IOS members and JET contributors, 'Benchmarking of codes for plasma burn-through in tokamaks,' *Nuclear Fusion*, vol. 60, no. 12, p. 126 049, 2020. DOI: 10.1088/1741-4326/abb95c.

[51] D. Bohm, 'The characteristics of electrical discharges in magnetic fields,' *Qualitative Description of the Arc Plasma in a Magnetic Field*, 1949.

[52] B. Lloyd, P. G. Carolan and C. D. Warrick, 'ECRH-assisted start-up in ITER,' *Plasma Physics and Controlled Fusion*, vol. 38, no. 9, p. 1627, 1996. DOI: 10.1088/0741-3335/38/9/007.

[53] V. T. G. Riccardo, P. L. Andrew, A. Sandford Kaye and P. Knoll, 'Disruption design criteria for Joint European Torus in-vessel components,' *Fusion Science and Technology*, vol. 43, no. 4, p. 493, 2003. DOI: 10.13182/FST03-A296.

[54] E. M. Hollmann *et al.*, 'Plasma–surface interactions during tokamak disruptions and rapid shutdowns,' *Journal of Nuclear Materials*, vol. 415, no. 1, Supplement, S27, 2011. DOI: https://doi.org/10.1016/j.jnucmat.2010.10.009.

[55] I. Svenningsson, O. Embreus, M. Hoppe, S. L. Newton and T. Fülöp, 'Hot-tail runaway seed landscape during the thermal quench in tokamaks,' *Phys. Rev. Lett.*, vol. 127, p. 035 001, 2021. DOI: 10.1103/PhysRevLett.127.035001.

[56] A. Jøsang, *Subjective logic: a formalism for reasoning under uncertainty*. Springer International Publishing, 2016, ISBN: 9783319423371.

[57] R. Garnett, *Bayesian Optimization*. Cambridge University Press, 2023. DOI: 10.1017/9781108348973.

[58] G. De Ath, R. M. Everson, A. A. M. Rahat and J. E. Fieldsend, 'Greed is good: Exploration and exploitation trade-offs in Bayesian optimisation,' *ACM Transactions on Evolutionary Learning and Optimization*, vol. 1, no. 1, p. 1, 2021. DOI: 10.1145/3425501.

[59] F. Nogueira, *Bayesian optimization: Open source constrained global optimization tool for Python*. https://github.com/fmfn/BayesianOptimization, 2014.

[60] S. C. Chiu, M. N. Rosenbluth, R. W. Harvey and V. S. Chan, 'Fokker-planck simulations of knock-on electron runaway avalanche and bursts in tokamaks,' *Nuclear Fusion*, vol. 38, no. 11, p. 1711, 1998. DOI: 10.1088/0029-5515/38/11/309.

[61] O. Embréus, A. Stahl and T. Fülöp, 'On the relativistic large-angle electron collision operator for runaway avalanches in plasmas,' *Journal of Plasma Physics*, vol. 84, no. 1, p. 905 840 102, 2018. DOI: 10.1017/S002237781700099X.

[62] E. M. Hollmann *et al.*, 'Study of argon assimilation into the post-disruption runaway electron plateau in DIII-D and comparison with a 1D diffusion model,' *Nuclear Fusion*, vol. 59, no. 10, p. 106 014, 2019. DOI: 10.1088/1741-4326/ab32b2.

Part II

Included papers

Paper A

Runaway electron generation during tokamak start-up

M. Hoppe, I. Ekmark, E. Berger and T. Fülöp

Journal of Plasma Physics **88** 905880317 (2022)

https://doi.org/10.1017/S002237782200054X

Paper B

Bayesian optimization of massive material injection for disruption mitigation in tokamaks

I. Pusztai, I. Ekmark, H. Bergström, P. Halldestam, P. Jansson, M. Hoppe, O. Vallhagen and T. Fülöp

Journal of Plasma Physics **89** 905890204 (2023)

https://doi.org/10.1017/S0022377823000193

Paper C

Fluid and kinetic studies of tokamak disruptions using Bayesian optimization

I. Ekmark, M. Hoppe, T. Fülöp, P. Jansson, L. Antonsson, O. Vallhagen and I. Pusztai

Journal of Plasma Physics **90** 905900306 (2024)

https://doi.org/10.1017/s0022377824000606

Paper D

Runaway electron generation in disruptions mitigated by deuterium and noble gas injection in SPARC

I. Ekmark, M. Hoppe, R. A. Tinguely, R. Sweeney, T. Fülöp and I. Pusztai

Accepted for publication in Journal of Plasma Physics.

https://arxiv.org/abs/2502.19891